

COMPTONIZATION IN SUPER-EDDINGTON ACCRETION FLOW AND GROWTH TIMESCALE OF SUPERMASSIVE BLACK HOLES

TOSHIHIRO KAWAGUCHI

LUTH, Observatoire de Paris, Section de Meudon, 5 Place J. Janssen, 92195 Meudon, France

Department of Physics and Astronomy, The University of Oklahoma, 440 West Brooks St., Norman, OK 73019, USA

Department of Astronomy, Graduate School of Science, Kyoto University, Sakyo-ku, Kyoto 606-8502, Japan

Postdoctoral Fellow of the Japan Society for the Promotion of Science

toshihiro.kawaguchi@obspm.fr

Received 2002 October 31; accepted 2003 April 19

ABSTRACT

Super-Eddington accretion onto black holes (BHs) may occur at Ultra-Luminous compact X-ray sources in nearby galaxies, Galactic microquasars and narrow-line Seyfert 1 galaxies (NLS1s). Effects of electron scattering (opacity and Comptonization) and the relativistic correction (gravitational redshift and transverse Doppler effect) on the emergent spectra from super-Eddington accretion flows onto non-rotating BHs are examined for $10^{1.5}$ and $10^{6.5} M_{\odot}$ BH masses (M_{BH}). With $\dot{m} [\equiv \dot{M}/(L_{\text{Edd}}/c^2)] \geq 100$, the spectral hardening factor via electron scattering is $\lesssim 2.3 - 6.5$. Due to the \dot{m} -sensitive hardening factor, the color temperature of the innermost radiation is not proportional to $L^{0.25}$, differing from the simplest standard accretion disk. The model is applied to optical-soft X-ray emission from NLS1s. We pick up one NLS1, namely PG 1448+273 with an inferred M_{BH} of $10^{6.4} M_{\odot}$, among the highest \dot{m} candidates. The broadband spectral distribution is successfully reproduced by the model with an extremely high \dot{m} (=1000) and the viscosity parameter α of 0.01. This implies that this object, as well as some other highest \dot{m} systems, is really young: the inferred age, M_{BH}/\dot{m} , is about 10^6 years. We also briefly discuss the distribution of \dot{m} for transient and highly variable NLS1s, finding that those are located at $3 \lesssim \dot{m} \lesssim 300$. Such a moderately high accretion rate is indicative of thermal instability. Furthermore, \dot{m} for a possible type-2 counterpart of NLS1s, NGC 1068, is found to be similar to \dot{m} for NLS1s.

Subject headings: accretion, accretion disks — black hole physics — galaxies: active — galaxies: nuclei — X-rays: galaxies — X-rays: stars

1. INTRODUCTION

Super-Eddington accretion phenomena onto black holes (BHs) may be important for formation and evolution of supermassive BHs. It may have been much more common in the young universe, when the average black hole mass (M_{BH}) would have been smaller than now. Such phenomena are possible sources of UV-Extreme UV (EUV) photons that may have governed the thermal and star formation history of the universe. Moreover, those extreme accretion rate phases provide us a laboratory in examining our knowledge on accretion phenomena, which have been studied intensively under sub-Eddington regimes (e.g., Shakura & Sunyaev 1973).

Some Ultra-Luminous compact X-ray sources (ULXs) and Galactic microquasars show large bolometric luminosity (\gtrsim the Eddington luminosity L_{Edd} of $1.4 M_{\odot}$) and high color temperature (~ 1 keV), often referred as T_{in} (e.g., Roberts & Warwick 2000; Makishima et al. 2000; Colbert & Ptak 2002). We note that recent results of ULXs obtained with *XMM-Newton* seem to show lower T_{in} (~ 0.15 keV; Miller et al. 2003). Some possible physical explanations for their nature, including rotating BHs, high accretion rate ($\dot{M} > L_{\text{Edd}}/c^2$, where \dot{M} is the gas accretion rate), intermediate BH mass ($\sim 100 M_{\odot}$) and beamed radiation (see, however, Misra & Sriram 2003) have been discussed.

There is a subclass of Active Galactic Nuclei (AGNs) that are candidates for super-Eddington accretion, namely narrow-line Seyfert 1 galaxies (NLS1s) and their luminous counterpart, narrow-line QSOs. They are characterized as follows (see Pogge 2000). (i) They have narrower Balmer lines of hydrogen (e.g., FWHM of $H\beta \leq 2000$ km s $^{-1}$), relative to usual broad-

line Seyfert 1 galaxies (BLS1s) and QSOs having FWHM of $H\beta \gtrsim 5000$ km s $^{-1}$ (e.g., Osterbrock & Pogge 1985). (ii) They often emit strong optical Fe II multiplets (e.g., Halpern & Oke 1987). (iii) Their optical-soft X-ray, big blue bump is hotter than BLS1s/QSOs: they have bluer optical spectra (Grupe et al. 1998) and often show steep and luminous soft X-ray excess (Pounds et al. 1996; Otani et al. 1996; Boller et al. 1996; Wang et al. 1996; Laor et al. 1997; Leighly 1999b). (iv) Rapid soft/hard X-ray variability is another characteristic of NLS1s (Otani et al. 1996; Boller et al. 1997; Leighly 1999a; Hayashida 2000). The soft X-ray spectral variability of NLS1s is opposite to that of BLS1s: spectra get harder when they become brighter (Cheng, Wei & Zhao 2002).

When the luminosity from the accretion disk/flow L becomes close to L_{Edd} [$\sim 1.3 \times 10^{45} (M_{\text{BH}}/10^7 M_{\odot})$ erg s $^{-1}$], it has been shown that the advective energy transport in the flow dominates over radiative cooling (Abramowicz et al. 1988; section 10.3 of Kato, Fukue & Mineshige 1998). Such a disk is called an the optically-thick ADAF (advection-dominated accretion flow) or slim disk, since it is moderately thick geometrically. Abramowicz et al. showed that L saturates at around a few times L_{Edd} when M exceeds L_{Edd}/c^2 , and that the flow shines even inside the marginally stable orbit [$3 r_{\text{Sch}}$ for non-rotating BHs; where r_{Sch} is the Schwarzschild radius and $r_{\text{Sch}} \equiv 2GM_{\text{BH}}/c^2 \simeq 3 \times 10^{12} (M_{\text{BH}}/10^7 M_{\odot})$ cm = $10^{-3} (M_{\text{BH}}/10^7 M_{\odot})$ lt-days.]. The physical reason why the advection turns on at super-Eddington regime will be the fact that photons can not escape from the flow before photons/gas are swallowed by the central BH (the photon trapping effect; Begelman & Meier 1982; we discuss it in §6.2). Slim disk models for ULXs have been constructed to explain High T_{in} (Watarai et al. 2000) and mysterious behaviors

in T_{in} v.s. L_X diagrams (Watarai, Mizuno & Mineshige 2001). Similarly, these models are successful in discussing strong soft X-ray emission (large T_{in} relative to other AGNs) and time variability of NLS1s (Mineshige et al. 2000, with M_{BH} and \dot{M} being free parameters). Currently, the most promising picture of NLS1s and narrow-line QSOs is that they contain relatively less massive black holes (with $M_{\text{BH}} \sim 10^{6-8} M_{\odot}$) and higher L/L_{Edd} (with $L \sim L_{\text{Edd}}$).

As to the emergent spectra from super-Eddington accretion, Szuszkiewicz, Malkan & Abramowicz (1996) and Wang et al. (1999) considered the opacity due to electron scattering, but without Comptonization nor the relativistic correction. Mineshige et al. (2000) and Watarai et al. (2000) simply apply the local blackbody approximation, whereas Watarai et al. (2001) take the spectral hardening factor of 1.7 from Shimura & Takahara (1995) in order to mimic the effect of Comptonization. We note that this factor is derived in the sub-Eddington regime, and thus the extent of Comptonization at super-Eddington phase is not evaluated by it (see §3.2). Self-irradiation and –occultation are discussed by Fukue (2000) with self-similar solutions of the slim disk model (e.g., Begelman & Meier 1982). Most recently, Wang & Netzer (2003) have studied the effect of Comptonization with self-similar solutions, in order to explain X-ray emission from NLS1s.

A big problem remains when we compare the slim disk model with the observed optical/UV–soft X-ray spectra of NLS1s. Namely the predicted soft X-ray is too steep compared with observations (Szuszkiewicz et al. 1996; Wang et al. 1999).

We examine the effects of electron scattering in opacity, of Comptonization and of the relativistic correction upon spectra from transonic slim accretion flows onto non-rotating BHs, in order to figure out to what extent those effects change the emergent spectrum and whether the effects are enough to fit the observed spectral energy distributions. Now that M_{BH} estimations for AGNs are accumulating, we are able to compare the models and observational data with less free parameters than previous studies. We have obtained a promising fit to the broad-band energy distribution for the first time. Methods and assumptions of the numerical calculations are given in §2. We then discuss the physical quantities and emergent spectra of the slim disk in §3. We turn to the comparison of the model with observed, broad-band spectra of NLS1s in the next section. The growth timescale of supermassive BHs is discussed in §5. In §6, several discussions are presented. The final section is devoted to a summary. Throughout the present study we use the normalization $\dot{M}_{\text{Edd}} (\equiv L_{\text{Edd}}/c^2)$ for \dot{M} :

$$\begin{aligned} \dot{M}_{\text{Edd}} &\simeq 1.3 \times 10^{18} (M_{\text{BH}}/10M_{\odot}) \text{ g s}^{-1} \\ &\simeq 1.3 \times 10^{24} (M_{\text{BH}}/10^7 M_{\odot}) \text{ g s}^{-1} \\ &\simeq 2.0 \times 10^{-2} (M_{\text{BH}}/10^7 M_{\odot}) M_{\odot} \text{ yr}^{-1}. \end{aligned} \quad (1)$$

Hereafter, \dot{m} refers to $\dot{M}/\dot{M}_{\text{Edd}}$.

Throughout this study, the luminosity is calculated from observed flux assuming isotropic radiation, zero cosmological constant, deceleration parameter $q_0 = 0.5$, and Hubble constant $H_0 = 75 \text{ km/s/Mpc}$.

2. NUMERICAL PROCEDURES

2.1. The Structure of the Accretion Disk

In order to discuss the shape of the emergent spectra from the innermost regions, it is essential to solve the full, derivative equations, rather than the self-similar solutions or other approximate solutions (based on a priori inner boundary conditions or

no regularity conditions). The transonic nature of the accretion flow should also be carefully treated.

We solve the steady-state, transonic accretion disk structure. The numerical methods are basically the same as those adopted in Matsumoto et al. (1984). The code has been extended for time-dependent simulations (Matsumoto, Kato & Honma 1989; Honma et al. 1991a,b) and it has been made use of in subsequent papers; Takeuchi (2000), Watarai et al. (2000, 2001) and Mineshige et al. (2000). Here, we summarize the numerical procedures, and briefly describe the basic equations in the following paragraphs. We employ the pseudo-Newtonian potential, $\psi = -GM/(r-r_{\text{Sch}})$ (Paczyński & Witta 1980), and cylindrical coordinates, (r, φ, z) .

In this study, we use vertically integrated (height-averaged) derivative equations. The scale-height of the disk H is comparable to radius r in the case of extremely large accretion rates $\dot{M} \gtrsim 100 L_{\text{Edd}}/c^2$. One may wonder if such a height-averaged approach would not be appropriate. The same problem arises in an optically thin ADAF (Narayan & Yi 1995; see section 10.2 of Kato et al. 1998 and references therein). Narayan & Yi (1995) found that the 2-dimensional solutions of the exact non-height-integrated equations agree quite well with those of the simplified height-integrated equations when the ‘height-integration’ is done along a constant spherical radius, rather than along z at constant cylindrical radius (see Narayan 1997). The height-integrated equations therefore are fairly accurate descriptions of quasi-spherical, advective flows.

We construct the vertically integrated equations, using the integrated variables, such as surface density, $\Sigma \equiv \int \rho dz = 2\bar{\rho}H$, and integrated total (gas plus radiation) pressure, $\Pi \equiv \int pdz = 2\bar{p}H$. Throughout this study (except for the absorption coefficient $\bar{\kappa}$), each quantity with a bar on top means the vertically averaged value, evaluated from the value at the mid plane (value with the suffix ‘mid’): $\bar{\rho} = (16/35)\rho_{\text{mid}}$, $\bar{p} = (128/315)p_{\text{mid}}$ and $\bar{T} = \frac{2}{3}T_{\text{mid}}$, respectively (Hōshi 1977; see Matsumoto et al. 1984). The scale-height of the flow H is determined by hydrostatic balance between the vertical gravity and pressure: i.e. $H = \Omega_K/c_s$, where c_s is the sonic speed. Equations for the conservations of the mass, momentum, and angular-momentum are

$$-2\pi r \Sigma v_r = \dot{M} = \text{const.}, \quad (2)$$

$$v_r \frac{dv_r}{dr} + \frac{1}{\Sigma} \frac{d\Pi}{dr} = \frac{\ell^2 - \ell_K^2}{r^3} - \frac{\Pi}{\Sigma} \frac{d\ln\Omega_K}{dr}, \quad (3)$$

and

$$\dot{M}(\ell - \ell_{\text{in}}) = -2\pi r^2 T_{r\varphi}, \quad (4)$$

respectively. Here, $\Omega (= v_{\varphi}/r)$, $\Omega_K [= (GM/r)^{1/2}/(r-r_{\text{Sch}})]$, $\ell (= rv_{\varphi})$, $\ell_K (\equiv r^2\Omega_K)$ and ℓ_{in} are respectively, the angular frequency of the gas flow, the Keplerian angular frequency in the pseudo-Newtonian potential, the specific angular momentum, the Keplerian angular momentum and the specific angular momentum finally swallowed by the BH. As to the viscous stress tensor we adopt the usual prescription $T_{r\varphi} \equiv -\alpha\Pi$ with the viscosity parameter α . Unless Otherwise noted, we apply α of 0.1. We neglect self-gravity of the disk, for simplicity. We will see that this is self-consistent with the computed density profile.

The energy budget (per unit surface area) at each radius is symbolically written as

$$Q_{\text{adv}}^- = Q_{\text{vis}}^+ - Q_{\text{rad}}^-, \quad (5)$$

where $Q_{\text{adv}}^- [\propto \Sigma v_r T(ds/dr)]$ is the advective cooling with s being specific entropy, and the other two terms on the right-hand

side represent viscous heating and radiative cooling, respectively. Assuming that the effective optical depth τ_{eff} is larger than unity, we apply the usual, diffusion approximation for Q_{rad}^- (cf. §3.1);

$$Q_{\text{rad}}^- = \frac{8acT_{\text{mid}}^4}{3\bar{\kappa}\rho_{\text{mid}}H} \approx \frac{Hu_{\text{rad}}}{t_{\text{diff}}}, \quad (6)$$

where the total opacity coefficient is $\bar{\kappa} = \kappa_{\text{abs}}^- + \kappa_{\text{es}}^-$. Here, u_{rad} and t_{diff} mean the radiation energy density per unit volume ($a\bar{T}^4$) and the diffusion time scale of photons (see §3.1), respectively. This equation describes the photon leakage. Neutrino leakage in proto-neutron stars is discussed in §6.2. If τ_{eff} gets smaller than unity, u_{rad} will be lower than $a\bar{T}^4$. The current cooling rate (eq. 6) will then overestimate the true cooling rate (Beloborodov 1998). An improvement of the formula, e.g., multiplying the cooling rate by $(1 - \exp^{-\tau_{\text{eff}}})$, would be required in the future.

The outer boundary conditions are imposed at $r = 2.0 \times 10^4 r_{\text{Sch}}$, where each physical quantity is taken from the formula of the standard disk (Shakura & Sunyaev 1973). The choice of the outer radius does not influence on the inner solutions (e.g., Abramowicz et al. 1988). The basic equations are integrated by the semi-implicit method from the outer boundary to the inner one taken at $r = 2.5r_{\text{Sch}}$ for $\dot{m} \leq 10$ and $1.01r_{\text{Sch}}$ for $\dot{m} \geq 100$. The solutions satisfy the regularity condition at the transonic radius, at about $2.7r_{\text{Sch}}$, and we adopt the free boundary conditions at the inner edge.

The system is taken to be a disk consisting of thermal plasma around a Schwarzschild black hole of mass M_{BH} . We also assume 1-Temperature gas (i.e., temperatures of protons and of electrons are the same). The Rosseland mean opacity is adopted for the absorption opacity κ_{abs} ; $\kappa_{\text{abs}}^- = \kappa_{\text{abs},0} \bar{\rho} \bar{T}^{-3.5}$. In this study, every optical depth is measured between the surface and the mid-plane of the flow (not from one surface to the other). Generally, the optical depth of absorption τ_{abs} ($H\bar{\rho}\kappa_{\text{abs}}^-$) is much less than that of electron scattering τ_{es} ($H\bar{\rho}\kappa_{\text{es}}^-$, with the electron scattering opacity κ_{es}^- of $0.4 \text{ cm}^2/\text{g}$) in the region of interest ($r \lesssim 10^{3.4} r_{\text{Sch}}$; cf. §3.2 in Kato et al. 1998). The flow is optically thick; $\tau_{\text{abs}} + \tau_{\text{es}} \gg 1$. The absorption opacity is an important factor when we are considering whether the effective optical depth of the flow [$\tau_{\text{eff}} \equiv \sqrt{3\tau_{\text{abs}}(\tau_{\text{abs}} + \tau_{\text{es}})}$; Rybicki & Lightman 1979] exceeds unity or not. To estimate the absorption coefficient $\kappa_{\text{abs},0}$ (mainly bound-free transitions for AGN disks with solar abundances; see e.g., Laor & Netzer 1989), we simply take 30 times the free-free absorption coefficient ($\kappa_{\text{ff},0}^- = 6.4 \times 10^{22} \text{ cm}^2/\text{g}$) for the super massive BHs, as is done in Czerny & Elvis (1987). For much smaller M_{BH} ($32 M_{\odot}$), we adopt $\kappa_{\text{ff},0}^-$ as $\kappa_{\text{abs},0}$. The timescale of Comptonization and that of Coulomb collisions are much shorter than the accretion timescale (Beloborodov 1998).

We neglect the gas evaporation from the disk (e.g., Meyer & Meyer-Hofmeister 1994), since it becomes weak when the gas accretion rate approaches the Eddington limit (Liu et al. 2002). The coronae above and beyond the disk are not included in this study. It will be necessary to consider them when applying the models to hard X-ray spectra (Wang & Netzer 2003).

In total, the input parameters required for the calculations are M_{BH} , \dot{M} and α .

2.2. Spectral Calculations

We follow Czerny & Elvis (1987) and Wandel & Petrosian (1988), in dealing with the effect of opacity of electron scattering (i.e. the modified blackbody) and the effect of the

energy exchange via Compton scattering (Comptonization). More precise treatments, including such as the effects of radiative transfer (see Shimura & Manmoto 2003), will be required for more detailed comparison of models and observations. Given the T_{eff} , the local spectrum $I_{\nu}(r)$ can be expressed by $I_{\nu}(r) = B_{\nu}(T)f_{\nu}(T,r)$, where $B_{\nu}(T)$ is the Planck function. Here, $f_{\nu}(T,r)$ is

$$f_{\nu}(T,r) = \frac{2[1 - \exp^{-\tau_{\text{eff}}(T,r)}]}{1 + \sqrt{[\tau_{\text{abs},\nu}(T,r) + \tau_{\text{es}}(r)]/\tau_{\text{abs},\nu}(T,r)}}, \quad (7)$$

where $\tau_{\text{abs},\nu}(T,r)$ is the optical thickness for absorption with a given temperature T at frequency ν , and the effective optical depth $\tau_{\text{eff},\nu}(T,r)$ is computed as $\sqrt{3\tau_{\text{abs},\nu}(T,r)[\tau_{\text{abs},\nu}(T,r) + \tau_{\text{es}}(r)]}$. The parenthesis including the exponential term takes into account the finite, effective optical depth of the flow. For low $\tau_{\text{eff},\nu}(T,r)$ ($\ll 1$), it describes the thermal bremsstrahlung from an optically thin medium. If the absorption opacity dominates over the opacity of electron scattering (and if the flow is effectively, optically thick), $f_{\nu}(T,r)$ is unity. The color temperature T is determined so that the surface emissivity does not change: $\int_0^{\infty} d\nu I_{\nu}(r) \equiv acT_{\text{eff}}^4/4\pi$.

A simple evaluation of the spectral hardening factor due to the modified blackbody is (Madej 1974):

$$\log_{10} \left(\frac{T_{\text{col}}}{T_{\text{eff}}} \right) \simeq -\frac{1}{8} \log_{10} \left(\frac{\tau_{\text{abs}}}{\tau_{\text{abs}} + \tau_{\text{es}}} \right). \quad (8)$$

Compton scattering is important when the Compton parameter $y = (4k\bar{T}/m_e c^2) \text{Max}(\tau_{\text{es}}, \tau_{\text{es}}^2)$ is greater than 1. However, below the last thermalization surface, where the effective optical depth measured from the surface equals unity, the energy exchange via Compton scattering will be statistically canceled due to the efficient absorption. Scattering above the surface is in question. Then, the relevant opacity for electron scattering, τ'_{es} , will be $\tau_{\text{es}}/\tau_{\text{eff}}$ for $\tau_{\text{eff}} > 1$ and τ_{es} for $\tau_{\text{eff}} < 1$:

$$\tau'_{\text{es}} = \frac{\tau_{\text{es}}}{\text{Max}(\tau_{\text{eff}}, 1)}. \quad (9)$$

Finally, the effective Compton-y parameter y_* is

$$y_* = \frac{4k\bar{T}}{m_e c^2} \text{Max}(\tau'_{\text{es}}, \tau'_{\text{es}}^2). \quad (10)$$

Comptonization will considerably modify the emergent spectrum if $y_* > 1$. The radial distribution of y_* increases inwards steeply, reaching a maximum at $\sim (3-5)r_{\text{Sch}}$, and it decreases inward (Wandel & Petrosian 1988). In the regime for which $\tau_{\text{es}} \gg \tau_{\text{abs}}$ and $\tau_{\text{eff}} > 1$,

$$y_* \propto \bar{T}^{4.5} \bar{\rho}^{-1} \left(\frac{\kappa_{\text{abs},0}^-}{\kappa_{\text{ff},0}^-} \right)^{-1}, \quad (11)$$

yielding a strong temperature dependency.

Photons generated at large optical depth undergo many scatterings and change their energy as a result of Comptonization. The effect on emergent spectra can be estimated by assuming that a fraction $f_{\text{th},\nu}$ of the photons at frequency ν are shifted and cumulated into a Wien peak of an average energy $3kT$. For a given frequency ν , the fraction of these thermalized photons to all generated photons $f_{\text{th},\nu}$ is given as

$$f_{\text{th},\nu} = \exp \left\{ -\frac{\ln(kT/h\nu)}{\tau_{\text{es}}^2 \ln[1 + 4kT/m_e c^2 + 16(kT/m_e c^2)^2]} \right\} \quad (12)$$

(Svensson 1984), if the absorption is negligible. For high-energy photons ($kT < h\nu$), $f_{\text{th},\nu}$ would be able to exceed unity.

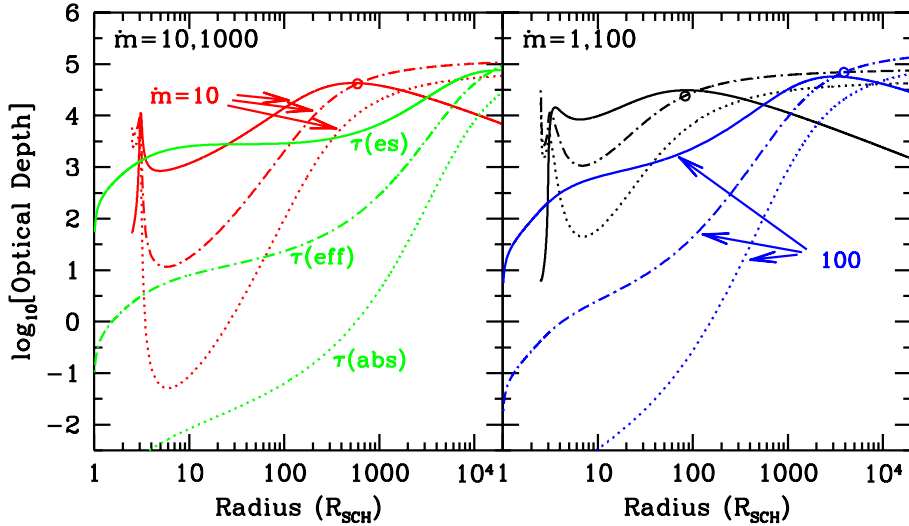


FIG. 1.— Opacity of electron scattering (τ_{es} , solid lines), that of absorption (τ_{abs} , dotted lines) and the effective opacity (τ_{eff} , dot-dashed lines). Here, M_{BH} and α are chosen to be $10^{6.5} M_{\odot}$ and 0.1, respectively. It is shown that τ_{es} is larger than τ_{abs} by several orders at $r \lesssim 10r_{\text{Sch}}$ for all the \dot{m} (1-1000). The left panel is drawn for $\dot{m} = 10$ and 1000, while the right one for $\dot{m} = 1$ and 100. Open circles indicate the position where $p_{\text{rad}} = p_{\text{gas}}$. Inner parts are p_{rad} -dominated regions. With $\dot{m} = 1000$, entire region presented here are p_{rad} -dominated.

We therefore put a constraint so that $f_{\text{th},\nu} \leq 1.0$. Since the redistribution of low-energy photons into Wien peak is the problem, this artificial constraint on high-energy photons will be a reasonable approximation (cf. Wandel & Petrosian 1988). The formula (eq. 12) can be adapted to a more general case if τ_{es} in the equation is replaced by the total optical depth $\tau_{\nu}^{\text{total}}$ (Czerny & Elvis 1987):

$$\begin{aligned} \tau_{\nu}^{\text{total}} &= \frac{\tau_{\text{es}} + \tau_{\text{abs},\nu}}{1 + \tau_{\text{eff}}} \\ &\approx \tau_{\text{es}} \quad (\text{for } \tau_{\text{eff}} \ll 1, \text{ and } \tau_{\text{es}} \gg \tau_{\text{abs}}) \\ &\approx \tau_{\text{es}}^{1/2} \tau_{\text{abs}}^{-1/2} \quad (\text{for } \tau_{\text{eff}} \gg 1, \text{ and } \tau_{\text{es}} \gg \tau_{\text{abs}}). \end{aligned} \quad (13)$$

The removed photons will result in a total additional energy output (we use $2.7kT$ instead of $3kT$, following Wandel & Petrosian 1988)

$$I_{\text{th},\nu} = 2.7kT \int_0^{\infty} d\nu f_{\text{th},\nu} \frac{I_{\nu}}{h\nu}. \quad (14)$$

The distribution of the shifted photons around the Wien peak is approximated by a blackbody spectrum with a normalization constant C given by

$$I_{\text{th},\nu} \approx C a c T^4 / 4\pi. \quad (15)$$

As a whole, the deviation of the emitted spectrum from a blackbody is finally described as

$$f_{\nu}(T, r) =$$

$$\frac{2[1 - \exp^{-\tau_{\text{eff}}(T, r)}]}{1 + \sqrt{[\tau_{\text{abs},\nu}(T, r) + \tau_{\text{es}}(r)]/\tau_{\text{abs},\nu}(T, r)}} [1 - f_{\text{th},\nu}] + C, \quad (16)$$

instead of $f_{\nu}(T, r)$ in eq. (7). Again, the temperature T ($\geq T_{\text{eff}}$) is adjusted to reproduce the original surface emissivity, so that the luminosity of the flow is conserved. As the result, the emergent spectra become harder than spectra based on the local blackbody approximation [$B_{\nu}(T_{\text{eff}})$; Czerny & Elvis 1987; Wandel & Petrosian 1988]. A hot surface layer will arise whose temperature T is much larger than T_{eff} , as seen in standard disks with $\dot{m} > 1$ (Shimura & Takahara 1993).

Next, we add the effects of the relativistic correction on the effective temperature T_{eff} and emergent spectra. Since only

the gravitational redshift and transverse Doppler shift (i.e. no Doppler boosting) are considered, the computational results correspond to face-on views of the flow. We assume that the rotational velocity v_{φ} is almost the same as the Keplerian velocity v_K . The consistency will be shown later with the calculated velocity field (§ 3.1). We employ the relativistic correction for the Keplerian disk (e.g., Kato et al. 1998, §3.5.3);

$$(1 + z_{r.c.}) = \left(1 - \frac{3r_{\text{Sch}}}{2R}\right)^{-1/2}. \quad (17)$$

We take $1 + z_{r.c.} = [\text{Max}(10^{-3}, 1 - 3r_{\text{Sch}}/2R)]^{-1/2}$, for the moment. The effective temperature T_{eff} becomes lower by $(1 + z_{r.c.})^{-1}$ [i.e., emissivity per surface area decreases by $(1 + z_{r.c.})^{-4}$], compared with the cases without the relativistic correction (e.g., Watarai et al. 2000, 2001; Mineshige et al. 2000).

We have applied this expression to describe the shape of the radiation spectrum emitted at every radius of the disk.

3. NUMERICAL RESULTS

In this section, we show the basic physical quantities in the accretion flow and emergent spectra for M_{BH} of $10^{6.5} M_{\odot}$ and $\alpha = 0.1$. For AGNs ($M_{\text{BH}} \gtrsim 10^6 M_{\odot}$), M_{BH} is now estimated by a couple of methods, and both of the inner and outer radii are observable at X-ray and optical/UV bands. We chose α of 0.1 in order to compare the $T_{\text{eff}}(r)$ profile and the resultant spectra with those in Mineshige et al. (2000). We also describe briefly the α -dependency using the $\alpha = 0.01, 10^{-3}$ results, as well as the M_{BH} -dependency comparing with $10^{1.5} (= 32) M_{\odot}$ BH results.

3.1. Physical Quantities of the Flow

Figure 1 exhibits the opacity of electron scattering (τ_{es}), that of absorption (τ_{abs}) and the effective opacity (τ_{eff}). Here, M_{BH} and α are chosen as $10^{6.5} M_{\odot}$ and 0.1, respectively. The figure clearly shows that τ_{es} (solid lines) at $r \lesssim 100r_{\text{Sch}}$ is larger than τ_{abs} (dotted lines) by several orders for all the \dot{m} (1-1000). The deviation is much more prominent in the super-Eddington phases than the sub-Eddington phase ($\dot{m} \lesssim 10$). Therefore, the local blackbody approximation must be modified, especially in the super-Eddington cases where τ_{es} enormously dominates

over τ_{abs} (see eq. [8]). With $\dot{m} \sim 100$, $\tau_{\text{eff}} \leq 1$ at $r \lesssim 4r_{\text{Sch}}$. Thus, the diffusion approximation for the cooling rate (eq. 6) will not be valid around this \dot{m} . We will therefore search for objects with even higher \dot{m} in §4.1. The surface density Σ is proportional to τ_{es} : Σ decreases with an increasing \dot{m} as far as $\dot{m} \leq 100$. As \dot{m} increases from 100 to 1000, Σ conversely increases (since v_r increases only slightly) and the density at the inner region ($r \lesssim 50r_{\text{Sch}}$) is also enlarged: both of τ_{es} and τ_{abs} get larger. Consequently, the effective optical depth with $\dot{m} = 1000$ recovers to above unity. Open circles exhibit the radii where the radiative pressure ($a\bar{T}^4/3$) equals to the gas pressure ($2k_B\bar{\rho}\bar{T}/m_H$). The former dominates over the latter within the inner region. The \dot{m} -dependency of the radius is similar to the standard disk ($\propto \dot{m}^{16/21}$).

We present the effective Compton- y parameter y_* (eq. 10) for various accretion rates. Each solid line in figure 2 shows the distribution of y_* as a function of radius r . The horizontal dotted line means $y_* = 1$, above which the spectral distortion due to Comptonization is crucial. The large increase of y_* along with the increase of \dot{m} arises from a decrease of $\bar{\rho}$ and an increase of \bar{T} from $\dot{m} = 10$ to 100–1000 (see fig. 5). Since $\bar{\rho} \propto M_{\text{BH}}^{-1}$ and $\bar{T} \propto M_{\text{BH}}^{-1/4}$ (as will be shown later), it is quite difficult to achieve a large y_* ($\propto \bar{T}^{4.5}\bar{\rho}^{-1}$; eq. 11) with sub-Eddington accretion rates for all relevant M_{BH} . In other words, the huge y_* ($\gg 1$) is obtainable only for super-Eddington cases.

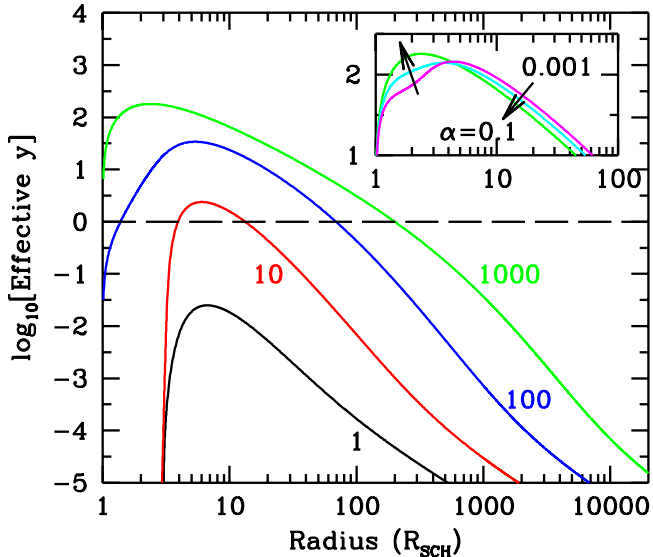


FIG. 2.— Effective Compton- y parameter, y_* , for various \dot{m} . A long-dashed line means that $y_* = 1$, above which Comptonization is very important on the spectral calculations. It is clear that y_* with super-Eddington accretion rate is much larger than the cases with sub-Eddington accretion. The inset shows the α -dependency of y_* for $\dot{m} = 1000$: $\bar{\rho}$ increases with smaller α , then y_* at the innermost region decreases.

We assume Keplerian rotation for the transverse Doppler effects (§2.2). Figure 3 shows the transverse velocity v_ϕ is almost equivalent to the Keplerian velocity v_K ($v_\phi \gtrsim 0.8v_K$) up to the extremely large \dot{m} (1000) cases. Thus, the assumption is not very bad. The radial velocity v_r increases with a larger \dot{m} (lower panel). This is the reason behind the ignition of the photon trapping in the super-Eddington accretion. In the extreme super-Eddington cases ($\dot{m} \gtrsim 1000$), v_r in the innermost region ($r \lesssim 10r_{\text{Sch}}$) is about 10% of the Keplerian one (i.e., $v_r \simeq \alpha v_K$). Thus, the inner flow could be more time variable than lower

\dot{m} cases. In the extreme limit of advection dominated flow ($Q_{\text{adv}}^- \gg Q_{\text{rad}}^-$), the radial velocity v_r is expected to be $\sim 0.4\alpha v_K$ (e.g., Fukue 2000). Filled dots indicate the location of the sonic point, where v_r equals to the sound speed c_s . The sonic points are located around $3r_{\text{Sch}}$ for all \dot{m} , being consistent with the $\alpha = 0.1$ cases in Abramowicz et al. (1988).

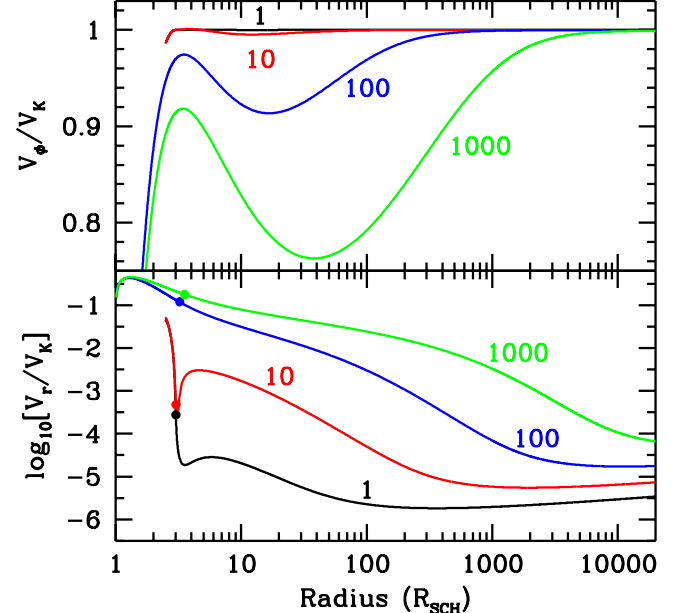


FIG. 3.— Azimuthal velocity (upper) and radial velocity (lower) in the unit of the Keplerian velocity v_K as functions of radius. The rotation is almost Keplerian for all the \dot{m} here, within $\sim 20\%$ deviation at most. The radial velocity increases drastically with increasing \dot{m} : it reaches $\sim 10\%$ of the Keplerian velocity for $\dot{m} = 1000$ at inner region ($r \lesssim 10r_{\text{Sch}}$). Filled dots indicate the location of the sonic points ($v_r/c_s = 1$) for each parameter set, where the sonic speed c_s is calculated as $\sqrt{\bar{p}/\bar{\rho}}$.

Next, we compare the timescales of accretion [t_{acc} defined as $(r - r_{\text{Sch}})/v_r$] with that of diffusion of photons from mid-plane to the surface of the disk [$t_{\text{diff}} \equiv H(\tau_{\text{es}} + \tau_{\text{abs}})/c$]. Figure 4 shows that t_{acc} is larger than t_{diff} everywhere for $\dot{m} \leq 10$, while it is not always true for $\dot{m} \geq 100$. The switch of the two timescales happens between \dot{m} of 10 and 100. Advective cooling (photon trapping) begins to take place from the inner region. For example, the outer part ($r > 40r_{\text{Sch}}$ for $\dot{m} = 100$ and $R > 400r_{\text{Sch}}$ for $\dot{m} = 1000$) does not suffer from the effects of photon trapping. Those radii can be analytically derived as $0.5\dot{m}$ (Begelman & Meier 1982). It is also clear that the accretion timescale at a fixed radius decreases drastically with increasing \dot{M} . In super-Eddington cases, the structure of the inner accretion flow can be highly time variable. The timescale for achieving the vertical hydrostatic balance, $H/c_s = \Omega_K^{-1}$, is always much shorter than t_{acc} .

The scale height of the flow H in the unit of radius r is shown in figure 5 (top panel). The aspect ratio H/r increases with \dot{M} , being geometrically thick ($H/R \gtrsim 0.5$) at $\dot{m} \gtrsim 100$. We shall discuss this issue later when we are seeking ideal objects to test the model (§4.1). Moreover, the shape of H/R shows that the heating by the irradiation from the innermost part of the flow onto the outer radii ($\gtrsim 10^4r_{\text{Sch}}$) is negligible. The radial profile of the mean density $\bar{\rho}$ is also shown (solid lines in the second panel). As Beloborodov (1998) noted, $\bar{\rho}$ at $r \lesssim 50r_{\text{Sch}}$ has a minimum at $\dot{m} \sim 100$. Here, the dot-dashed line indicates a

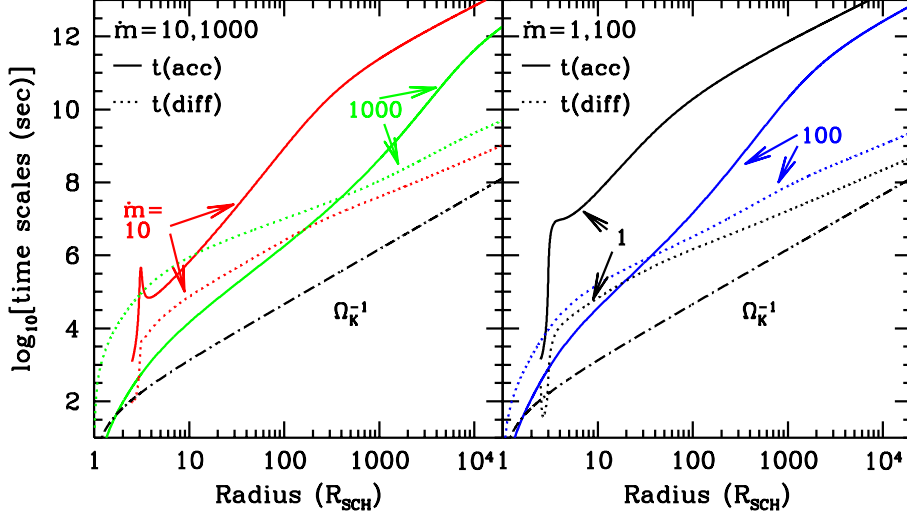


FIG. 4.— Accretion timescale ($t_{\text{acc}} = (r - r_{\text{Sch}})/v_r$; solid lines) and diffusion timescale of photons ($t_{\text{diff}} = H(\tau_{\text{es}} + \tau_{\text{abs}})/c$; dotted) for the slim accretion disk model. The viscosity parameter α is 0.1 here. The switch of the two time scale happens at \dot{m} between 10 and 100. The dot-dashed lines mean the vertical, hydrodynamical timescale [$H/c_s = \Omega_K^{-1} = 255(M_{\text{BH}}/10^7 M_{\odot})(r/3r_{\text{Sch}})^{0.5}(r/r_{\text{Sch}} - 1)$ sec for the Pseudo-Newtonian potential].

critical density, $\rho(\text{sg}, z)$, above which self-gravity of the disk in the vertical (z) direction must be considered:

$$\rho(\text{sg}, z) = \Omega_K^2 / (4\pi G) = 18(M_{\text{BH}}/10^7 M_{\odot})^{-2}(r/3r_{\text{Sch}})^{-1} (r/r_{\text{Sch}} - 1)^{-2} \text{ g/cm}^3. \quad (18)$$

As \dot{m} increases, the relative importance of self-gravity [$\rho(\text{sg}, z)/\bar{\rho}$] in the outer region is enhanced. With $\dot{m} > 1000$, the outer part of the flow [$r \gtrsim 2 \times 10^4 r_{\text{Sch}} \simeq 0.006(M_{\text{BH}}/10^{6.5} M_{\odot})\text{pc}$] will form a self-gravitating disk. Objects with super-Eddington accretion rate are therefore good laboratories for studying the self-gravity of accretion flows by optical/Near-IR observations. Quantitative details will be shown in a future paper (Kawaguchi, Pierens, & Huré 2003). Another critical density for radial self gravity, $\rho(\text{sg}, r)$ is $16\rho(\text{sg}, z)$ (Goldreich & Lynden-Bell 1965; see Huré 1998 for a review). The inertia of the heat (Beloborodov, Abramowicz & Novikov 1997; dashed lines in the second panel) is always much smaller than the gas rest mass density $\bar{\rho}$ in this study (disks around non-rotating BHs): $\rho_{\text{rad}} \equiv a\bar{T}^4/c^2 \simeq 10^{-11}(\bar{T}/10^6 \text{ K})^4 \text{ g/cm}^3 \ll \bar{\rho}$ (third panel).

Finally, the effective temperature profiles $T_{\text{eff}}(r)$ before the relativistic correction (solid lines) are compared with those with the correction (dotted lines; eq. 17). Although the flow with $\dot{m} > 100$ extends much closer to the central BHs than lower \dot{m} cases, those regions are not so luminous as thought in the previous papers (Watarai et al. 2000, 2001; Mineshige 2000). If the system is not face-on, the discrepancy of the two profiles shrinks due to the Doppler boosting and the reduction of transverse Doppler effect. Viewing-angle dependent spectra are needed for investigation in the future. The dashed line also shows $T_{\text{eff}}(r)$, but it is derived without advection (i.e., $Q_{\text{vis}}^+ = Q_{\text{rad}}^-$):

$$T_{\text{eff}}(r) = 6.2 \cdot 10^5 \left(\frac{M_{\text{BH}}}{10^7 M_{\odot}} \right)^{-1/4} \left(\frac{\dot{M}}{L_{\text{Edd}}/c^2} \right)^{1/4} \left(\frac{r}{r_{\text{Sch}}} \right)^{-3/4} \left(1 - \sqrt{\frac{3r_{\text{Sch}}}{r}} \right)^{1/4} \text{ K.} \quad (19)$$

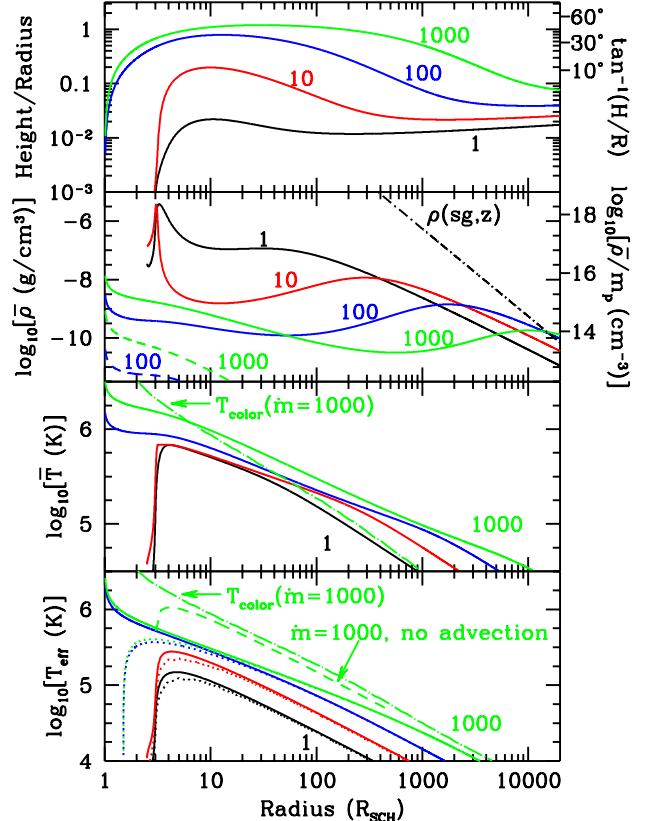


FIG. 5.— Examples of \dot{m} -dependency of the physical quantities. The corresponding \dot{m} are labeled. First, the scale height of the flow (from the mid-plane to the surface) divided by the radius is shown (top). The second panel exhibits the radial profile of the mean density $\bar{\rho}$ by solid lines. The dot-dashed line indicates a critical density, $\rho(\text{sg}, z)$, above which self-gravity of the disk in the vertical (z) direction must be considered. Lower two dashed lines mean the inertia of the heat, ρ_{rad} , for $\dot{m} = 100$ and 1000. The third panel depicts the mean temperature \bar{T} . In the bottom, the effective temperature profiles $T_{\text{eff}}(r)$ before the relativistic correction (solid lines) are compared with those with the correction (dotted lines; eq. 17) are shown. Dashed line also shows $T_{\text{eff}}(r)$, but it is the case with no advection (i.e., $Q_{\text{vis}}^+ = Q_{\text{rad}}^-$). Due to the relativistic correction, the maximum T_{eff} of the slim disk is less than that of the $Q_{\text{vis}}^+ = Q_{\text{rad}}^-$ case. Dot-long-dashed lines in the third and forth panel present the color temperature derived with eq. 16 for the $\dot{m} = 1000$ case. The spectral hardening factor can be estimated from the ratio of the color temperature to the effective temperature.

Due to the relativistic correction, the maximum T_{eff} of the slim disk becomes less than that of the $Q_{\text{vis}}^+ = Q_{\text{rad}}^-$ case. Dot-long-dashed lines in the third and forth panels present the color temperature derived with eq. 16 for the $\dot{m} = 1000$ case.

Since we shall use the spectra with α of 0.01 ($M_{\text{BH}} = 10^{6.5} M_{\odot}$) when testing our model with the observed spectrum, we here briefly discuss the α -dependency of the flow. The α -dependencies of all the physical quantities (figures 1–5) are almost the same as the standard disk: i.e., $\tau_{\text{es}}(\propto \Sigma) \propto \alpha^{-1}$, $v_r \propto \alpha$, t_{acc} and t_{diff} are proportional to α^{-1} , $H/r \propto \alpha^0$, $\bar{\rho} \propto \alpha^{-1}$, $\bar{T} \propto \alpha^{-0.25}$, etc. The exception arises at the innermost region, $r \leq 10r_{\text{Sch}}$. Namely, $\tau_{\text{es}}(\propto \Sigma)$, v_r and the two timescales at $r \leq 1.5r_{\text{Sch}}$ are unchanged. The transition between the two different α -dependencies occurs at $1.5 \leq r \leq 10r_{\text{Sch}}$. The effective Compton-y parameters for the three values of α (with $\dot{m} = 1000$) are drawn in the inset of fig 2, showing the decrease of y_* at $r \lesssim 4r_{\text{Sch}}$ with decreasing α . Figure 6 depicts the aspect ratio (top), $\bar{\rho}$ (second), \bar{T} (third), and T_{eff} (bottom) for different α (0.1, 0.01, 10^{-3}) with $M_{\text{BH}} = 10^{6.5} M_{\odot}$ and $\dot{m} = 1000$. The behavior of \bar{T} of the inner region is the opposite to that of the outer part. Lower α makes the self-gravity of the flow more important at outer radii. The sonic point approaches the center with decreasing α , as shown in Abramowicz et al. (1988). With smaller α , $\bar{T}(r)$ tends to have a hump, so that the pressure gradient [$d\Pi/dr \propto d(H\bar{T}^4)/dr$] pushes the gas towards the central BH more strongly. The α -dependency of $T_{\text{eff}}(r)$ is shown in Watarai & Mineshige (2001).

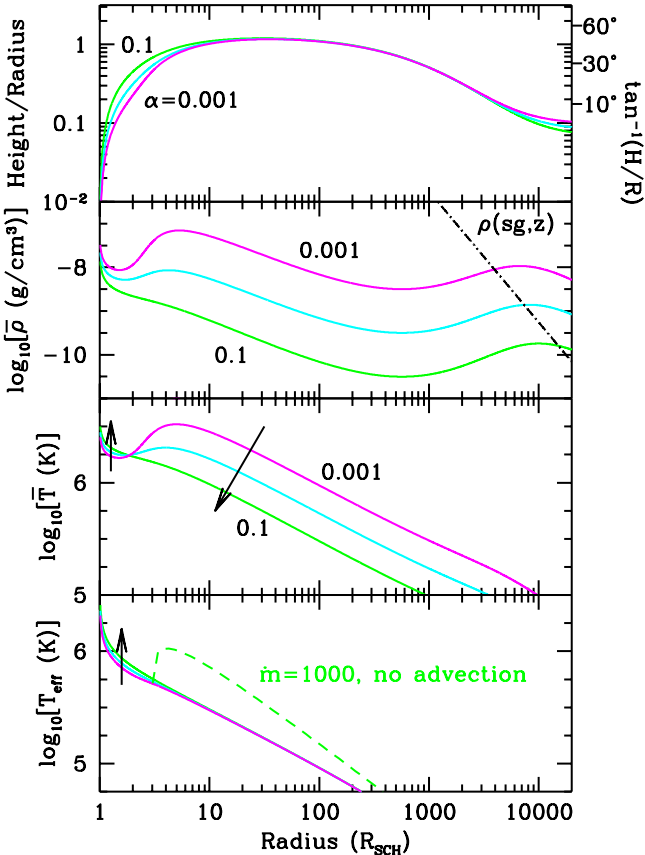


FIG. 6.— Aspect ratio (top), $\bar{\rho}$ (second), \bar{T} (third), and T_{eff} (bottom) for different α (0.1, 0.01 and 10^{-3}) with $M_{\text{BH}} = 10^{6.5} M_{\odot}$ and $\dot{m} = 1000$. The α -dependency of the physical quantities are almost the same as the standard disk, except for the innermost region, $r \lesssim 10r_{\text{Sch}}$. The behavior of \bar{T} of the inner region with varying α is the opposite to that of the outer part. Arrows mean the evolution with increasing α .

Computations for $M_{\text{BH}} = 32M_{\odot}$ are also made in order to 1) assess the M_{BH} dependency, 2) apply the present model to ULXs/microquasars, and 3) compare our spectra with those in Shimura & Takahara (1995) in the sub-Eddington regime. Although the \dot{m} -dependency of the quantities (figures 1–5) in the slim disk is different from the standard disk, the M_{BH} -dependency is almost identical: e.g., $H/r \propto M_{\text{BH}}^0$, $\bar{\rho}$ (at the p_{rad} -dominated region) $\propto M_{\text{BH}}^{-1}$, \bar{T} (p_{rad} region) and T_{eff} are proportional to $M_{\text{BH}}^{-1/4}$, t_{acc} and t_{diff} (p_{rad} region) are proportional to M_{BH} , etc. The radius (in the unit of r_{Sch}) at which $p_{\text{rad}} = p_{\text{gas}}$ is proportional to $M_{\text{BH}}^{2/21}$.

Different values of the ratio ($\kappa_{\text{abs},0}/\kappa_{\text{ff},0}$) are used in different M_{BH} cases (§2.1), thus absorption-dominated region is located farther out than for $M_{\text{BH}} = 10^{6.5} M_{\odot}$. Due to the change of the absorption coefficient, it gets easier for the flow to have τ_{eff} less than unity: $\tau_{\text{eff}} \leq 1$ at $r \leq 10r_{\text{Sch}}$ for $\dot{m} = 100$, and at $r \leq 3r_{\text{Sch}}$ for $\dot{m} = 1000$. Comparing with $10^{6.5} M_{\odot}$ black holes, y_* is enlarged by a factor of ~ 100 at all radii and all the \dot{m} . The changes of $\bar{\rho}$ and \bar{T} due to the decrease of M_{BH} by 5 orders result only in 0.6 order increase of y_* (eq. 11). The rest (~ 1.5 orders) arises from the decrease of ($\kappa_{\text{abs},0}/\kappa_{\text{ff},0}$). Since $\rho(\text{sg}, z) \propto M_{\text{BH}}^{-2}$, self-gravity of the disk around $32 M_{\odot}$ black holes is not important at all. Instead, it gets more significant with larger M_{BH} . Again, p_{rad} is always negligible.

3.2. Emergent Spectra

Figure 7 shows the each effect of spectral calculation on the emergent spectrum for the case of $\dot{m} = 1000$ and $\alpha = 0.1$. First, the dotted line represents the case with no advection: all the dissipated energy goes into radiation as in the standard accretion disks. For this curve, we put the inner radius at $3r_{\text{Sch}}$. The long-dashed line exhibits the spectrum with advection based on transonic accretion flow (i.e., the same as Mineshige et al. 2000, except for face-on view here). We note that the local spectrum is still assumed as blackbody radiation here. Next, we take into account the relativistic correction at the innermost region of the flow (dot-dashed line). The flow extends inside the last stable orbit ($3r_{\text{Sch}}$; e.g., Abramowicz et al. 1988; Watarai et al. 2000; Mineshige et al. 2000). However, the emission from those regions, where gravity is extraordinarily strong and azimuthal velocity is relativistic, is drastically suppressed by the gravitational redshift and transverse Doppler redshift. As the result, the color temperature of the inner region (where the highest energy photons are emitted) decreases by a factor of ~ 5.7 . We should stress here that the bolometric luminosity of the flow L is not very large in spite of the super-Eddington accretion rate; $L \sim 2.6L_{\text{Edd}}$ for the relativistic corrected spectrum while it is $5.1L_{\text{Edd}}$ for the non-corrected spectrum.

Next, we add the effect of electron scattering on opacity (i.e., the modified blackbody spectrum; short-dashed line). Finally, Comptonization is included in the computations (solid line). Radiation from the inner region is boosted towards higher energy by a factor of ~ 3.4 (the ratio of the color temperature to the effective temperature, called as the “spectral hardening factor”; see. e.g., Shimura & Takahara 1995) in comparison with the dot-dashed line. This factor can be estimated if one compares the color temperature (dot-long-dashed line) and the effective temperature (solid line) in the bottom panel of fig. 5. With the effects of electron scattering (opacity and Comptonization), we get more gradual slopes in soft X-ray compared with the original spectra (dotted line and long-dashed

line). The effect of Comptonization is included in the slim disks for the first time here (see also Shimura & Manmoto 2003 and Wang & Netzer 2003).

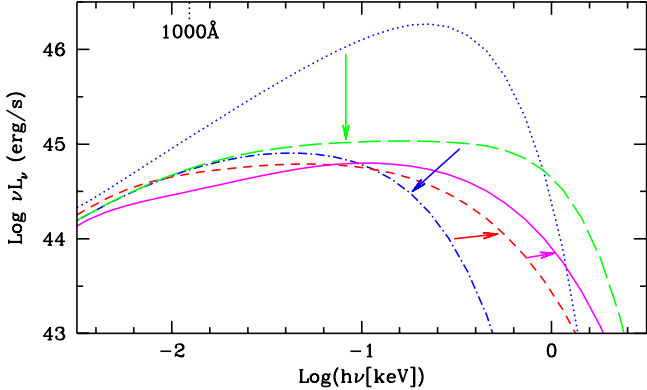


FIG. 7.— Each effect on the emergent spectrum for $\dot{m} = 1000$. The dotted line represents the case with no advection (as in the standard accretion disks) with an assumed inner radius at $3r_{\text{Sch}}$. Then, the long-dashed line exhibits the spectrum with advection based on the transonic accretion flow (i.e., the same as Mineshige et al. 2000, except for face-on view here), and the bolometric luminosity of the flow L is about $5.1 L_{\text{Edd}}$. The local spectrum is still assumed as blackbody radiation here. Next, we take into account the relativistic correction at the innermost region of the flow (dot-dashed line). As the result, the color temperature of the emission from the innermost region decreases by a factor of ~ 5.7 , and L becomes to be $2.6 L_{\text{Edd}}$. More, we add the effect of electron scattering on opacity (i.e., modified blackbody spectrum; short-dashed line). Radiation from the inner region is boosted towards higher energy. Finally, Comptonization is included in the computations (solid line). Comparing the solid and dot-dashed lines, the spectral hardening factor (the ratio of the color temperature to the effective temperature) at the innermost region is about 3.4.

For the spectrum with all the effects ($\dot{m} = 1000$ and $\alpha = 0.1$), the contribution from each radial component is shown in figure 8; $r \geq 10^3$, $r = 10^3\text{--}100$, $100\text{--}10$, $10\text{--}5$, $5\text{--}3$ and $r \leq 3r_{\text{Sch}}$, respectively (thin solid lines). For comparison, we also draw the spectra without the effects of electron scattering (but with the relativistic correction) by thin dot-dashed lines. The spectral hardening factor of each spectrum is 1.3, 1.7, 2.3, 2.9, 3.4 and 4.0 for each radial region, respectively. This means that the inner emission suffers more spectral shift by electron scattering.

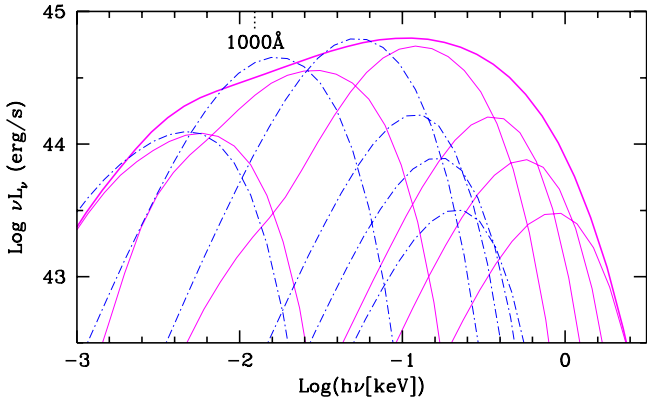


FIG. 8.— Contributions from different radii; $r \geq 10^3$, $r = 10^3\text{--}100$, $100\text{--}10$, $10\text{--}5$, $5\text{--}3$ and $r \leq 3r_{\text{Sch}}$, from left to right respectively, for $M_{\text{BH}} = 10^{6.5} M_{\odot}$, $\dot{m} = 1000$ and $\alpha = 0.1$. Thick solid line shows the spectrum from the entire radii with all the spectral effects as same as in fig. 7, while 6 thin-solid lines mean the spectra from the different radial regions above. For comparison, we also draw the spectra without the effects of electron scattering (but with the relativistic correction) by thin dot-dashed lines. The “spectral hardening factor” of each spectrum is 1.3, 1.7, 2.3, 2.9, 3.4, 4.0 for each radial region, respectively.

Figure 9 shows the α -dependency of the emergent spectra with $\alpha = 0.1$, 0.01 and 10^{-3} . The arrows indicate the change of spectra with increasing α . The meanings of two kinds of lines (solid and dot-dashed) are the same as fig. 7. Without the effects of electron scattering, the spectra are almost identical. Spectral boosting by electron scattering is quite α sensitive. Since $\tau_{\text{es}}/\tau_{\text{abs}} \propto \alpha^{1/8}$, an increase of α results in an increase of the surface temperature T (eq. 16), so we get more spectral boosting. Previous models with the effect of electron scattering in opacity (Szuszkiewicz et al. 1996; Wang et al. 1999) employ a low viscosity parameter $\alpha = 0.001$, in order to guarantee that the flow is effectively optically thick. Such a low α means that the spectral distortion by electron scattering is very small (fig. 9).

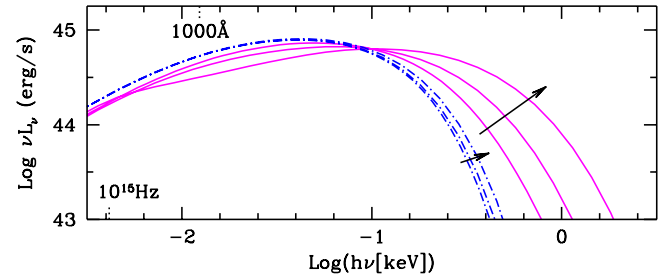


FIG. 9.— Spectra with three different values of α : $\alpha = 0.1$, 0.01 and 10^{-3} . The arrows indicate the change of spectra with increasing α . The meanings of two kinds of lines (solid and dot-dashed) are the same as in fig. 7. Without the effects of electron scattering, the spectra are almost identical. Spectral boosting by electron scattering is quite α sensitive.

Figure 10 shows the emergent spectra with $M_{\text{BH}} = 32M_{\odot}$ and $\alpha = 0.1$. Meanings of the lines are the same as in fig. 7. Those spectra can correspond to those of some ULXs/microquasars. The spectral hardening factors are around 1.3, 1.9 and 6.5 for $\dot{m} = 1$, 10 and 1000 , respectively. For $\dot{m} = 100$, it is quite difficult to measure it, since the spectrum is highly distorted (see §4.2 for the reason). The \dot{m} -dependency presented here is qualitatively the same as the $10^{6.5} M_{\odot}$ results. Some more details are shown in §4.2. Due to the reduction of $(\kappa_{\text{abs},0}/\kappa_{\text{ff},0})$ in the $10^{1.5} M_{\odot}$ calculations (§2.1), the effects of electron scattering upon spectral boosting are enhanced relative to $10^{6.5} M_{\odot}$ results (fig. 7 and fig. 12). Shimura & Takahara (1995) derived the spectral hardening factors to be ~ 1.7 for $\dot{m} = 1$ and ~ 1.9 for $\dot{m} = 10$, using the radiative transfer computations including Comptonization. It is often assumed that the vertical distribution of the heating rate is proportional to the volume gas density (Ross, Fabian & Mineshige 1992; Shimura & Takahara 1993, 1995). Our results are consistent with their values, and thus the method used here for spectral calculations seems to work quite well. Strong disk Comptonization, which is turned on at very high state in a couple of microquasars, is suggested by Kubota (2001) and Kubota, Makishima & Ebisawa (2001b). We note that the inferred bolometric luminosity assuming the standard $T_{\text{eff}}(r)$ profile (e.g., Mitsuda et al. 1984) will be underestimating the true disk luminosity (perhaps by a factor of 1.5–2), since super-Eddington accretion flows have flatter (in νL_{ν} plot) spectra than the standard accretion disk (fig. 10).

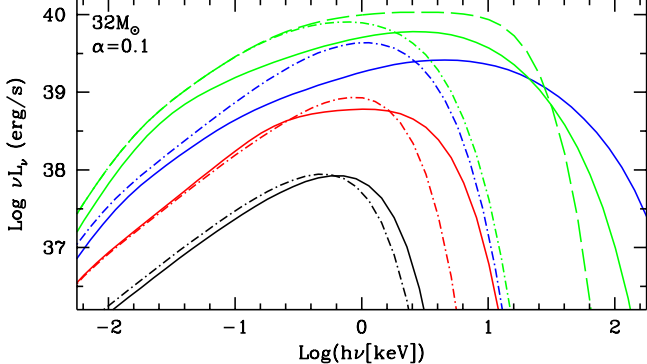


FIG. 10.— Emergent spectra from the face-on slim disks (solid lines) with $M_{BH} = 32M_{\odot}$ and $\alpha = 0.1$. Accretion rates \dot{m} used for the computations are 1, 10, 100 and 1000 from bottom to top, respectively. The meanings of lines are the same as in fig. 7. Roughly, the spectral hardening factor is 1.3, 1.9 and 6.5 for $\dot{m} = 1, 10$ and 1000, respectively. Shimura & Takahara (1995) reported that the spectral hardening factor $\simeq 1.7$ for $\dot{m} = 1$, and $\simeq 1.9$ for $\dot{m} = 10$ ($M_{BH} = 1.3 - 10M_{\odot}$), with a weak M_{BH} -dependency ($\sim M_{BH}^{0.1}$).

4. OBSERVATIONAL TESTS OF THE MODEL

Here, we will test the models with the data of AGNs, for which detailed data at both optical/UV and X-ray bands are available, and some sorts of M_{BH} estimations have been developed.

4.1. The Object Ideal for The Test

Objects ideal for the test should have the highest \dot{m} , since we expect the largest difference in spectral shape from the spectrum of the standard accretion disk. Also, the high \dot{m} indicates a geometrically thick accretion flow (figure 5), then the self-obscuration may happen (Fukue 2000). If we observe the innermost region of those highest \dot{m} objects (detections with soft X-ray will indicate it), it implies that we are looking at the flow almost face-on. Thus, we can neglect the longitudinal Doppler effect (Doppler boosting), which is an annoying effect in the model fitting. [We simply estimate the luminosity as $4\pi d_L^2 \times \text{flux}$, neglecting the inclination of the disk/flow. The inferred luminosity will overestimate the true luminosity somewhat in the case of a concave flow-geometry due to the self-irradiation (Fukue 2000; Misra & Sriram 2003).] Another reason to favor a large \dot{m} is that the effective optical depth of the flow with \dot{m} of 100 can be smaller than 1, so the radiative cooling rate (eq. 6) would not be accurate in that case. We should select even higher \dot{m} objects. Another requirement for ideal test objects is that they should also harbor as small M_{BH} as possible. Small enough M_{BH} allows the accretion disk to become hot enough for the emission from the innermost part of the flow to be easily observable in the soft X-ray band.

In terms of the temporal analysis, low M_{BH} selection is also desirable in order to recognize the temporal behavior characteristic of the slim disk. The accretion timescale at $r \lesssim 10$ and $\lesssim 30 R_{\text{Sch}}$ will have the order of a typical exposure time of X-ray satellite (~ 10 k sec) for $\dot{m} = 100$ and 1000, respectively (Figure 4). Thus, the slim disk is expected to change its dynamics within one observation. To select the candidates for high \dot{m} and low M_{BH} objects, we plot B -band luminosity of each active nuclei $\nu L_{\nu}(B)$ as a function of M_{BH} as follows.

There are several ways to estimate M_{BH} of AGNs. (1) the reverberation mapping technique provides physically meaningful M_{BH} estimation [$M_{BH}(\text{rev})$; e.g., Kaspi et al. 2000],

though the method is quite time consuming (an order of a year). Now, $M_{BH}(\text{rev})$ estimations for AGNs whose FWHM(H β) less than 2000 km/s have been obtained for 9 objects (Kaspi et al. 2000). (2) An easier way is the one assuming some photo-ionization models for H β lines [$M_{BH}(\text{ph})$; Wandel, Peterson & Malkan 1999]. The two estimations agree with each other quite well. The method utilizes the regression line between the size of broad line regions R_{BLR} and $\nu L_{\nu}(5100 \text{ \AA})$, determined in the reverberation mapping (Kaspi et al. 2000): $R_{\text{BLR}} = 32.9 [\nu L_{\nu}(5100 \text{ \AA}) / (10^{44} \text{ erg/s})]^{0.7}$ lt-days. (3) Nelson (2000) and Ferrarese et al. (2001) found that the [O III] line width or the stellar velocity dispersion, σ , is correlated with $M_{BH}(\text{rev})$ in AGNs, and that they overlap the bulge mass-to-BH mass correlation in non-active galaxies (Gebhardt et al. 2000; Ferrarese & Merritt 2000). Thus, the [O III] width also provides an estimate of M_{BH} , $M_{BH}(\text{[O III]})$. We use the regression reported as the equation 2 in Wang & Lu (2001), that was derived from $M_{BH}(\text{rev})$ or $M_{BH}(\text{ph})$ v.s. [O III] width of the narrow-line and broad-line AGNs: $M_{BH}(\text{[O III]}) = 10^{7.78} [\text{FWHM}(\text{[O III]}) / 2.35 / (200 \text{ km/s})]^{3.32} M_{\odot}$. We confirmed that an alternative regression (eq. 3) in Wang & Lu (2001) does not change the result significantly.

There is some scatter around the regression lines, both in the R_{BLR} v.s. $\nu L_{\nu}(5100 \text{ \AA})$ diagram and in the M_{BH} v.s. [O III] width plot. To minimize uncertainty, we estimate M_{BH} from the geometric mean of the three estimations, namely the square root of the product of $M_{BH}(\text{rev})$ and $M_{BH}(\text{[O III]})$, or that of $M_{BH}(\text{ph})$ and $M_{BH}(\text{[O III]})$. In general, those evaluations agree with each other quite well: $\langle (\log_{10} M_{BH}(\text{rev or ph}) - \log_{10} M_{BH}(\text{[O III]}))^2 \rangle = 0.54$. The SDSS Early Data Release spectra also show a similar scatter: $\sigma \simeq 0.67$ in $\log_{10} M_{BH}(\text{ph})$ (Boroson 2003). In some objects without two available estimations, we use either of the three¹.

For some NLS1s, the [O III] line can be deconvolved into two components (Véron-Cetty, Véron, & Goncalves 2001, and references therein), namely the broad, blueshifted one and the narrower one with the same redshift as other lines. The latter seems to arise from clouds showing normal galactic rotation. For $M_{BH}(\text{[O III]})$, the latter [O III] width is used as Wang & Lu (2001) did, if the [O III] line is deconvolved into the two components. However, for I Zw I, it is known that neither of the two components appear at the galaxy redshift (Phillips 1976; Véron-Cetty et al. 2001): both components seem to show outflows. Therefore, this object is omitted in our plot.

In general, NLS1s have a narrower [O III] line width ($\lesssim 300$ km/s) than BLS1s. To take account of a possible overestimation of the [O III] width due to the moderate spectral resolution (~ 200 km/s), Wang & Lu (2001) divide the [O III] width listed in Véron-Cetty et al. (2001) by a factor of 1.3. We follow the same procedure. Spectroscopic observations with higher spectral resolution and, as for I Zw I, a careful analysis on the two [O III] components will be required in the future to obtain a regression with smaller scatter.

In addition to the objects and data in Wang & Lu (2001), Nelson (2000) and Kaspi et al. (2000), the following, well-known NLS1s that are not tabulated in the literatures are added; namely, several NLS1s with the ASCA observations (see Leighly 1999b). Some NLS1s show giant amplitude (a factor of $\sim 10-100$) X-ray variability. We also add such objects into our sample (see §6.1 for more details). Table 1 lists the added

¹ $M_{BH}(\text{[O III]})$ for IC 3599 and 2E 1346+2646 and $M_{BH}(\text{rev})$ for PG 0052+251, PG 1226+023, PG 1426+015, PG 1617+175 and PG 1700+518.

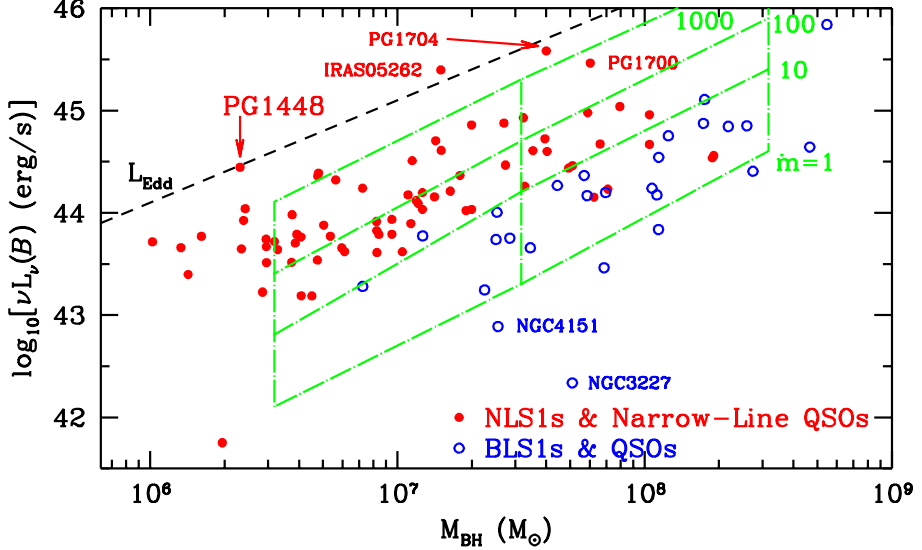


FIG. 11.— B-band luminosity of active nuclei as a function of M_{BH} . Data are derived from Wang & Lu (2001), Nelson (2000) and Kaspi et al. (2000). NLS1s and narrow-line QSOs are denoted by filled circles, while BLS1s and QSOs are plotted by open circles. Narrow-line objects show higher \dot{m} than broad-line objects on average. Among the small M_{BH} , higher \dot{m} NLS1s, PG 1448+273 is the candidate with highest \dot{m} . Then, this object can be desirable to test the overall slim disk model. Dashed lines are loci computed by the model for different \dot{m} with $\alpha = 0.1$. Optical flux has a very weak α -dependency (fig. 9). Absolute B -band magnitude M_B of -23 corresponds to $\nu L_{\nu}(B)$ of $10^{44.8}$ erg/s.

objects; 8 objects from Leighly (1999b) and 4 from Grupe, Thomas & Beuermann (2001). In total, we have 100 objects; 74 narrow and 26 broad objects. We note that the current sample is far from a complete sample by any means.

The Galactic extinction is corrected using a standard extinction curve (Savage & Mathis 1979). For all the conversion between optical bands and for the K -correction, it is assumed that $f_{\nu} \propto \nu^{-0.5}$ (e.g., Kaspi et al. 2000). Accuracy of the optical photometric data must be considered carefully: e.g., the nuclear fraction of the measured luminosity is 0.64–0.97 for

$\nu L_{\nu}(B) \geq 10^{44.2}$ erg/s sources (Surace, Sanders & Evans 2001). Less luminous sources would contain less nuclear fraction. The optical variability is of smaller amplitude than X-ray variability.

Figure 11 exhibits the M_{BH} v.s. $\nu L_{\nu}(B$ -band) plot. This plot will be useful to estimate the order of \dot{m} (roughly $\propto L_{\nu}(B)/M_{\text{BH}}$) in a sample of objects. The closer to the line of L_{Edd} (dashed line), the higher \dot{m} such objects will have. NLS1s/narrow-line QSOs seem to have higher \dot{m} than BLS1s/QSOs. If we do not apply the [O III]–width correction by a factor of 1/1.3 for the Wang & Lu (2001) sample,

TABLE 1
ADDITIONAL NLS1S AND A BLS1

Objects Name	z	$H\beta^a$ FWHM (km/s)	m_V (ref.)	A_V^b	$[\text{O III}]^a$ FWHM (km/s)	L_B^c	R_{BLR} (lt-day)	M_{BH}^d (ph)	M_{BH}^d ([O III])
PHL 1092	0.396	1790	17.0(VV01)	0.13		45.0	168.2	7.90	
RX J0439.7-4540	0.224	1010	16.6(G99)	0.03	1020	44.7	92.2	7.14	8.90
NAB 0205+024 .. (Mrk 586)	0.155	1050	15.4(K91)	0.10		44.9	125.0	7.30	
PKS 0558-504 ..	0.137	1250	15.0(R86)	0.15		44.9	140.6	7.51	
1H 0707-495	0.041	1050	15.7(R86)	0.32	1516 ^e	43.7	18.5	6.47	
IRAS 13224-3809	0.067	650 ^f	15.2(Y99)	0.23	810	44.3	47.8	6.47	8.56
IRAS 13349+2438	0.108	2200	14.3(M95)	0.04		45.0	147.4	8.02	
IRAS 20181-2244	0.185	370	16.8(ES94)	0.24	537	44.5	71.0	6.15	7.97
RX J0134.2-4258	0.238	900	16.0(G99)	0.06	670	45.0	150.6	7.25	8.29
WPVS 007	0.029	1620	14.8(G99)	0.04	320	43.6	17.0	6.81	7.23
RX J2217.9-5941.	0.160	1850	16.2(G99)	0.08	1075	44.6	77.0	7.59	8.97
RX J2349.3-3125.	0.135	5210	16.6(G99)	0.05	475	44.2	46.0	8.26	7.80

^a Line widths of $H\beta$ and [O III] are taken from Leighly (1999b) for the objects above the horizontal line, and from Grupe et al. (1999), with $\sim 5\text{\AA} \sim 300$ km/s resolution, for the lower objects.

^b Galactic extinction A_V is derived from NED.

^c $\log_{10}(\nu L_{\nu}(B)[\text{erg/s}])$

^d $\log_{10}(M_{\text{BH}}/M_{\odot})$

^e This [O III] width is uncertain due to low [O III] flux and contamination from Fe II blends (Leighly 2001, private communication). Then, we estimate M_{BH} from $M_{\text{BH}}(\text{ph})$ alone.

^f This $H\beta$ width may be underestimated, since there seems some contamination of narrow $H\beta$ line arises from starburst of the host galaxy (Leighly 2001, private communication).

REFERENCES.— G99: Grupe et al. 1999; K91: Korista 1991; R86: Remillard et al. 1986; VV01: Véron-Cetty & Véron 2001; Y99: Young et al. 1999; M95: Mason et al. 1995; ES94: Elizalde & Steiner 1994

most NLS1s (54 out of 74) shift to the right (larger M_{BH}) by 0.2 dex. Still there is the systematic difference of \dot{m} between NLS1s/narrow-line QSOs and BLS1s/QSOs. The objects' names are indicated for several outliers. PG 1700 and PG 1704 are also pointed out as the highest \dot{m} objects by Collin et al. (2002) who estimated \dot{m} of 34 AGNs from the optical luminosity and $M_{\text{BH}}(\text{rev})$.

The best, high \dot{m} , low M_{BH} target is PG 1448+273 ($z = 0.065$). The inferred BH masses are $M_{\text{BH}}(\text{ph}) = 8.4 \times 10^6 M_{\odot}$ and $M_{\text{BH}}(\text{O III}) = 6.3 \times 10^5 M_{\odot}$. We thus estimate M_{BH} as $10^{6.4} M_{\odot}$. It has $\nu L_{\nu}(B) = 10^{44.4} \text{ erg/s}$. The FWHM width of H_{β} and [O III] are 820–1050 km/s and 155 km/s, respectively (Stirpe 1990; Véron-Cetty et al. 2001). The optical spectrum shows no evidence for contamination from the host galaxy into the optical luminosity, and it is not expected in B -band (Stirpe 1990). These widths are still narrower than typical NLS1s, indicating that this object will be one of the extreme NLS1s. We expect the object will show the hottest accretion disk among the sample, which will enable us to investigate the nature of accretion flow unprecedentedly well with soft X-ray observations (*XMM-Newton*). No X-ray observations have been performed for this object except for ROSAT All Sky Survey (RASS); the 0.1–2 keV photon index Γ is 3.2 ± 0.3 (1σ), and $\nu F_{\nu}(2 \text{ keV})$ is $1.4 \pm 0.5 \times 10^{-12} \text{ erg/s/cm}^2$ (Walter & Fink 1993). There are no special remarks on this object in Grupe et al. (2001) where some objects showing strange variability during RASS observations are reported.

4.2. Comparison of the Models with the Available Data

Now, we compare our model spectra (§3.2) with the currently available, observed data of PG 1448+273 at optical–Soft X-ray bands (Figure 12). The standard disk model ($\dot{m} \lesssim 10$) does not fit the broadband spectrum of PG 1448+273 (dot and a tie-bow error), and thus a slim disk model is required. The Soft X-ray photon index of PG 1448+273 ($\Gamma \sim 3.2$) is larger than normal BLS1s (see e.g., Boller et al. 1996), but is not the largest one among the NLS1s ($\Gamma \sim 2.5$ –4.5).

Figure 12 exhibits a comparison of spectra between the optical (B -band)–soft X-ray (by RASS) observations and the models. Here, M_{BH} is taken to be $10^{6.5} M_{\odot}$, and $\alpha = 0.1$ (top) or $\alpha = 0.01$ (bottom). The corresponding \dot{m} value for each line is shown in the figure. The spectral hardening factors for $\alpha = 0.1$ cases are ~ 1.2 , 1.3 and 3.4 for $\dot{m} = 1$, 10 and 1000, respectively, while $\alpha = 0.01$ results indicate the factor to be ~ 2.8 and 2.3 for $\dot{m} = 100$ and 1000, respectively. The $\dot{m} = 1000$ and $\alpha = 0.1$ model with all the effects (solid line) has a problem: the soft X-ray spectrum is too boosted towards higher energy to explain the observed value. We found that the PG 1448+273 data is well fitted by a model with an extremely large accretion rate; $\dot{m} = 1000$ and $\alpha = 0.01$. As far as the soft X-ray spectrum is concerned, both of the $\dot{m} = 100$ and 1000 models with $\alpha = 0.01$ can fit the data. Thus, it is very important to look at both of optical/UV and soft X-ray bands. We note that most of the dissipated energy is advected and swallowed into the BH as trapped photons. This is the first example where optical–soft X-ray spectral distribution of NLS1s are explained by models. The dashed lines are the curves based on the previous computation of the slim disk (Mineshige et al. 2000) with $\dot{m} = 1000$, which turned out to have difficulty in explaining the soft X-ray luminosity/spectral slope. In the bottom panel, spectra with an additional hard X-ray power-law are also shown, for presentation purpose. The photon index of 2.15 (Brandt et al. 1997;

Leighly 1999b), with the 3000Å–2 keV spectral index of 1.6 (Brandt, Laor & Willis 2000) are used.

Figure 12 also exhibits the \dot{M} dependence of the model spectra with a fixed M_{BH} . We recall that $\tau_{\text{eff}} \leq 1$ at the inner region, with $\dot{m} = 100$ and $\alpha = 0.1$. Because of the exponential term in eq. 16 (the effect of the finite τ_{eff}), the surface temperature T drastically increases with the parameter set. The spectral hardening factor, the degree of spectral boosting, relative to the model without electron scattering is indeed enhanced and becomes more strongly radius-dependent (see Shimura & Takahara 1995, §3.4 for r -dependency of the factor in sub-Eddington AGN disks) in the $\dot{m} = 100$ case than the $\dot{m} = 1000$ result. Up to $\dot{m} \leq 10$, the peak frequency of the disk emission (T_{in}) varies with \dot{M} in a similar fashion to that of the standard accretion disk: $T_{\text{in}} \propto M_{\text{BH}}^{-1/2} \dot{M}^{1/4} \propto M_{\text{BH}}^{-1/4} \dot{m}^{1/4}$. Above that accretion rate, there is a jump in T_{in} , due to the \dot{m} -sensitive spectral boosting via electron scattering. Such a jump does not happen without electron scattering effects (dot-dashed lines).

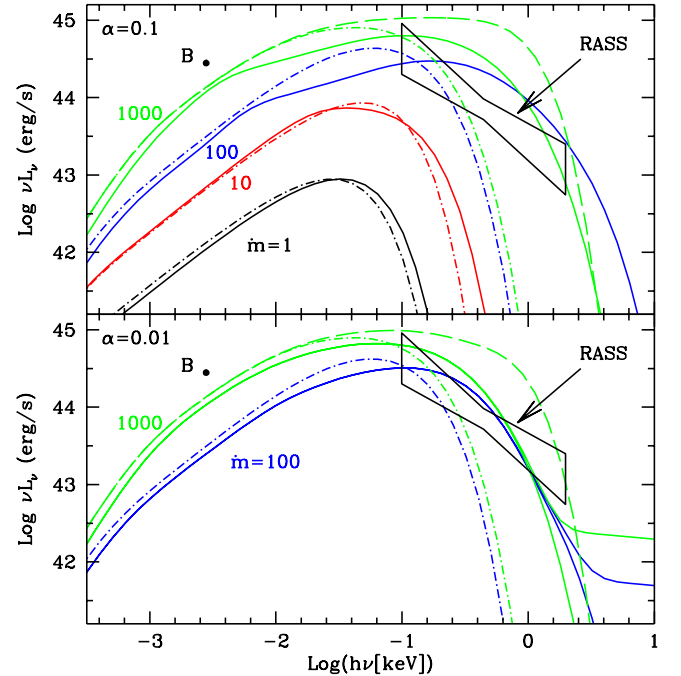


FIG. 12.— Spectral models of the face-on slim disk (solid lines), with $M_{\text{BH}} = 10^{6.5} M_{\odot}$, for the observed data of PG 1448+273 (a dot and a tie-bow; errors indicate 1σ of Γ and flux). Accretion rate used for the computations are labeled. Bolometric luminosities L are 0.021, 0.21, 1.2 and 2.6 of L_{Edd} for $\dot{m} = 1, 10, 100$ and 1000, respectively. The meanings of lines are the same as in fig. 7. The dot-dashed and long-dashed lines are computed without the effects of electron scattering: the relativistic correction is taken into account in the former, while not in the latter. Top: The cases with $\alpha = 0.1$. Roughly, the spectral hardening factor is 1.2, 1.3 and 3.4 for $\dot{m} = 1, 10$ and 1000. (For $\dot{m} = 100$ it is difficult to measure it, since the spectrum is highly distorted. See the text for that reason.) To reproduce the optical flux, $\dot{m} \geq 1000$ is required. The $\dot{m} = 1000$ model with all the effects (solid line) has a problem: the soft X-ray spectrum is too boosted towards higher energy to explain the observed value. Bottom: The same as above, except for $\alpha = 0.01$ here. Models for $\dot{m} = 100, 1000$ are shown, with the resultant spectral hardening factor of ~ 2.8 and 2.3, respectively. For presentation purpose, we add a hard X-ray power-law with a photon index of 2.15 for each spectrum, with the 3000Å–2 keV spectral index of 1.6. It is found that the $\dot{m} = 1000$ case reproduce the observed broad-band spectrum quite well.

With $\dot{m} \geq 100$, T_{in} saturates, as found in previous works (Wang et al. 1999; Watarai et al. 2000; Mineshige et al. 2000).

As shown above, we have established that the slim disk

model is promising for PG 1448+273 for B-band and RASS data ($\dot{m} = 1000$ producing $2.6 \times L_{\text{Edd}}$). This is the first success in reproducing optical–soft X-ray emission simultaneously. To verify and constrain our model further, we need a much higher signal-to-noise ratio and a broader band pass obtainable with *XMM-Newton*. We will show the detailed comparison between the model and the data, which will be obtained by our approved observation (PI; T. Kawaguchi), in a future paper. Also, whether we are able to fit the spectra at different flux states with the same M_{BH} provides a strong constraints on the accretion models.

4.3. Predicted X-ray Features

Below, we state several features predicted by the model. These properties will be judged by future observations.

Is the spectrum distorted due to electron scattering?

The most distinguishable feature of the slim disk is the soft X-ray spectrum (soft excess or soft X-ray hump) from the innermost region of the disk. The soft excess may not be fitted well by the so called multi-color disk spectra, since the slim disk model predicts that the soft X-ray emission is significantly distorted due to the strong radius-dependent, spectral hardening factor at a certain range of \dot{m} ($\dot{m} = 100$ with $\alpha = 0.1$; fig. 12 top panel). Such a power-law-like soft excess was recently reported in a couple of NLS1s, Ton S 180 (Vaughan et al. 2002) and Mrk 478 (Marshall et al. 2003) with $\Gamma \sim 3$ and ~ 1.5 for soft and hard X-ray, respectively.

Intrinsic spectral features

The temperature of the innermost region of NLS1s with $\dot{m} \gtrsim 1000$ seems to be around 10^6 K. Those objects tend to have weaker corona than coronae of low \dot{m} objects. Then, it can be possible to observe the intrinsic spectral features (bound-free and bound-bound) of the accretion flow in the soft X-ray band. Such features have commonly been attributed to “warm absorbers”. However, the strong Comptonization (fig. 2) may smear those features (see Shimura 2000). Some discussions upon possible disk emission features in *XMM* data have appeared recently (Branduardi-Raymont et al. 2001; Mason et al. 2003).

Does the color temperature change with flux?

The color temperature of the radiation from the innermost disk (T_{in}) may vary with flux significantly (Figure 12). Such a behavior of the slim disk (significant change of T_{in} associated with less change in L) is expected to occur at $\dot{m} = 10\text{--}100$, due to the \dot{m} -sensitive electron scattering. If we detect the significant T_{in} change, distinct from the simplest (without the effects of electron scattering) standard disk model ($T_{\text{in}} \propto L^{1/4}$), it is an evidence for strong electron scattering, and hence (see fig. 2) it is an indication of super-Eddington accretion in NLS1s.

It should be stressed that a similar T_{in} -change has been observed in ULXs/microquasars (see Makishima et al. 2000): e.g., Mizuno et al. (2001) found that three ULXs exhibit $T_{\text{in}} \propto L^{1/2}$, which is different from the relation in the standard disk, $T_{\text{in}} \propto L^{1/4}$.

Is Photon trapping important or does convection dominate?

Another expectation from the slim disk model is that the soft excess might be reduced at higher \dot{m} due to advection (photon trapping). The accretion timescale will become shorter than the timescale of photon diffusion (fig. 4). We may therefore expect less soft X-ray excess-to-optical flux ratio for extremely high \dot{m} than for a moderately large \dot{m} case. That could be verified from the combination of OM and EPIC observations, since

optical/UV radiation suffers less from the photon trapping. Absence of this effect will mean that the convective energy transport in the disk is more efficient than the radiative one.

5. GROWTH TIMESCALE OF BHS

The elapsed time since the gas-fueling started will have the order of M_{BH}/\dot{M} ($= 0.5 \dot{m}^{-1}$ Gy) unless a sudden change of accretion rate occurs. Thus, NLS1s and narrow-line QSOs could be the key objects for figuring out what turned on the efficient gas-accretion towards the central BHs. As described in the previous section, we found that some of them, including PG 1448+273, have an extremely high accretion rate: $\dot{m} \approx 1000$. This implies that the object is really young: its age inferred from M_{BH}/\dot{M} is about 10^6 years. Due to the rapid growth of M_{BH} , such a high \dot{m} stage will be a quite short phase.

It may be important to note that some ULXs exhibit extended optical nebulae (Pakull & Mirioni 2002). Assuming that a nebula is a remnant of a supernova-like event, they estimate the age of one ULX as ~ 1 Myr based on the size of the nebula (~ 400 pc in diameter), expansion velocity and $\text{H}\beta$ luminosity.

6. DISCUSSION

6.1. Highly Variable AGNs

Some NLS1s show giant amplitude (a factor of $\sim 10\text{--}100$) X-ray variability; short-term (\lesssim a day) variabilities in IRAS 13224-3809 (Boller et al. 1997; see also Otani et al. 1996), PHL 1092 (Forster & Halpern 1996; Brandt et al. 1999), RX J2217.9-5941 (Grupe et al. 2001), and Mrk 766 (Leighly et al. 1996; Grupe et al. 2001), as well as long-term (\sim years) variabilities in NGC 4051 (Guainazzi et al. 1998; Uttley et al. 1999), RE J1237+264 (= IC 3599; Brandt et al. 1995; Grupe et al. 1995a; Komossa & Bade 1999), 1H 0707-495 (Leighly et al. 2002) and WPVS 007 (Grupe et al. 1995b), etc. To investigate the physics and nature behind these phenomena, we have added such objects into figure 11; 3 NLS1s, WPVS 007 ($=$ IRXS J003915.6-511701; Grupe et al. 1995b), RX J0134.2-4258 (Grupe et al. 2000), RX J2217.9-5941 and one BLS1 RX J2349.3-3125 (Grupe et al. 2001). RX J1304.2+0205, HS1702+32 (Grupe et al. 2001) are not included since there are no optical data available.

When \dot{m} goes up, a shorter accretion timescale is associated with a higher radial velocity (Figure 3 and 4). This suggests that such specific NLS1s (and one BLS1) might have the highest \dot{m} among all NLS1s. Some of the highly variable and transient AGNs (e.g., NGC 4051) may be relevant to obscuration (e.g., Brandt & Gallagher 2000)

The resultant distribution of those AGNs are shown in Figure 13 together with other objects. It turns out that they do not belong to the highest \dot{m} group. This is true even if we use one specific M_{BH} estimation among the three, rather than the geometric mean. Instead, it seems that such highly-variable objects are located at the intermediate region where the two classes merge ($3 \lesssim \dot{m} \lesssim 300$). If this is true, the distribution may indicate that such high-amplitude variability is linked with a transience between a standard disk and a slim disk due to the thermal instability (Honma et al. 1991a,b; Leighly et al. 2002). Further studies with a sample including more transient NLS1s are required to examine this hypothesis.

Janiuk, Czerny & Siemiginowska (2002) discuss the thermal instability in terms of transitions of microquasars. Transitions seen in some ULXs (Kubota et al. 2001a) can also be relevant to the instability.

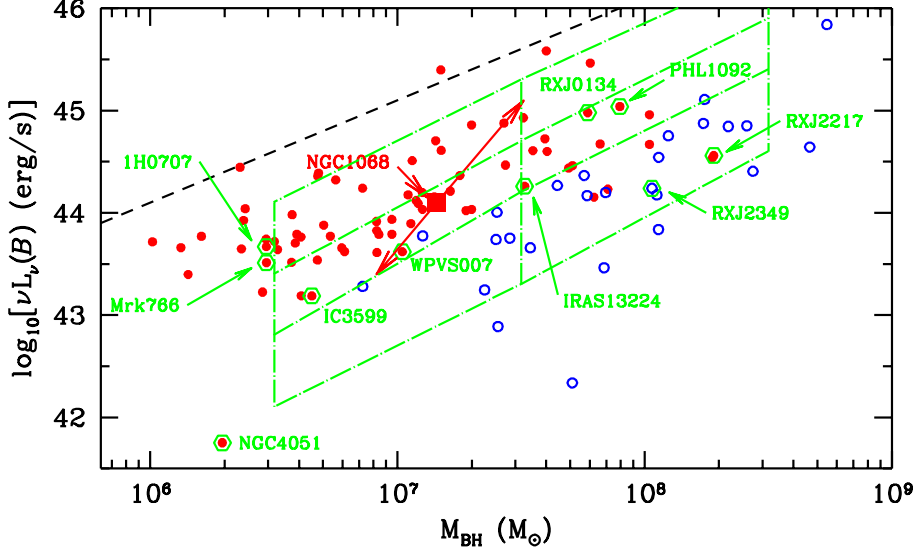


FIG. 13.— Resultant distribution of highly variable/transient AGNs (hexagonal dots). They do not belong to the highest \dot{m} group. Instead, it seems that such objects are located at the intermediate region where the two classes merge. A large filled square denotes NGC 1068 (§6.3).

6.2. Photon Trapping

As shown in fig. 4, the diffusion timescale of photons becomes longer than the accretion timescale (photon trapping). We expect that the diffusion approximation (eq. 6) should provide a reasonable estimation for the cooling rate, although Ohsuga et al. (2002) argue that it might not always be true for super-Eddington accretion rates. A similar trapping phenomenon can be seen for the neutrino trapping in a newly born neutron star (proto-neutron star) associated with a Type II (core-collapse) supernova. The diffusion timescale of neutrinos from the dense core (seconds) is longer than the dynamical timescale of collapse or bounce shock around the neutrino-sphere (1–10 ms; see Burrows 1990 for a review). Numerous studies (e.g., Janka & Hillebrandt 1989; Mezzacappa et al. 1998, etc), adopting the (flux-limited) diffusion approximation and Monte-Carlo simulations to treat the neutrino leakage, have been made for calculating the inner structure and light curve of the neutrino flux from a (convective) proto-neutron star. The long history of this field would help to consider the cooling rate in super-Eddington accretion flows.

The inner structure of a magnetized accretion flow will be highly inhomogeneous (e.g., Machida et al. 2000; Kawaguchi et al. 2000). Photons inside the flow tend to escape by passing through a low-density region (see Begelman 2001). Therefore, the degree of photon trapping, and thus that of advection, might be reduced when we take this into account. However, the photon diffusion timescale (dotted lines in fig. 4) is much longer than the dynamical timescale (Ω_K^{-1} ; dot-dashed line). Since the inner inhomogeneity will change within the timescale of Ω_K^{-1} , photons will still have difficulty in escaping from the flow. A lower α enhances the deviation of the two timescales.

6.3. NGC 1068; a Type 2 NLS1?

Here, we briefly discuss the accretion rate of a well-known Seyfert 2 galaxy, NGC 1068. The relatively narrow $H\beta$ line and significant FeII multiplets in the polarized emission from NGC 1068 (Miller, Goodrich, Mathews 1991) lead people to suspect it as a type 2 counterpart of NLS1s.

For NGC 1068, the mean [OIII] width (~ 1150 km/s) can not

be used for M_{BH} determination, since NLR clouds seem to suffer from the interaction with the jet (Dietrich & Wagner 1998). The lowest FWHM (~ 200 km/s) [OIII] clouds seem to be consistent with rotation around the nucleus, and the FWHM width of the line complex from those clouds is about 210km/s (Dietrich & Wagner 1998). Consequently, the implied $M_{\text{BH}}(\text{[O III]})$ is $4.2 \times 10^6 M_{\odot}$. Also, its polarized $H\beta$ line width is ~ 3000 km/s (Miller et al. 1991), and its intrinsic optical luminosity $[\nu L_{\nu}(B)]$ was estimated as $\sim 10^{44.1} (f_{\text{refl}}/0.01)^{-1}$ erg/s, assuming the fraction of nuclear flux reflected into our line of sight f_{refl} to be 0.01 (Pier et al. 1994). Therefore, $M_{\text{BH}}(\text{ph}) = 5.1 \times 10^7 (f_{\text{refl}}/0.01)^{-0.7} M_{\odot}$. The geometric mean is $10^{7.2} (f_{\text{refl}}/0.01)^{-0.35} M_{\odot}$. We note that f_{refl} is thought to be between 0.05 (Bland-Hawthorn, Sokolowski, Cecil 1991) and 0.001 (Bland-Hawthorn & Voit 1993). The inferred M_{BH} is consistent with the M_{BH} estimated from water masers in the central pc, $(1-2) \times 10^7 M_{\odot}$ (Greenhill & Gwinn 1997).

The filled square in Figure 13 indicates the location of NGC 1068, showing that it indeed has a high \dot{m} as NLS1s. The error-bar shown here arises from the uncertainty of f_{refl} alone.

6.4. Comparison with The QSO Composite Spectrum

NLS1s are the dominant source of diffuse EUV photons in the local universe (Edelson et al. 1999). To examine the contribution of NLS1s in the distant, young universe, we need to understand the shape of the EUV spectrum as functions of M_{BH} and \dot{M} .

In order to recognize the difference in spectral energy distributions between NLS1s and QSOs, we plot the QSO composite spectrum by dotted lines (Zheng et al. 1997; Laor et al. 1997; Telfer et al. 2002) upon our model spectra ($M_{\text{BH}} = 10^{6.5} M_{\odot}$, $\dot{m} = 100$ and 1000 with $\alpha = 0.01$) in figure 14. Following Laor et al. (1997), the vertical normalization of the composite spectrum is chosen to match with a representative NIR luminosity of nearby PG quasars, but re-adopting a Hubble constant of 75 km/s/Mpc (namely we divide by 2.25 from the spectrum in figure 6 of Laor et al. 1997). Although the $\dot{m} \sim 1000$ period will be a quite short phase and thus rare, the phase with $\dot{m} \sim 100$ will be common in NLS1s and narrow-line QSOs (fig. 11). As shown in figure 14, the two types of objects (NLS1s and QSOs)

show quite different distributions. The ratio of the EUV luminosity to optical ones or EUV to X-ray ratio are really different in the high \dot{m} systems and QSOs. The EUV luminosity is comparable in the $\dot{m} = 1000$ case and the QSO spectrum, while the EUV spectral slopes are not similar. The slope in EUV band plays an important role in indicating to what extent EUV photons penetrate into primordial gas clouds against self-shielding (e.g., Tajiri & Umemura 1998). Similar comparison can be seen when one plots the QSO composite spectrum onto the broadband spectrum of another NLS1, Mrk 478, in Marshall et al. (1996).

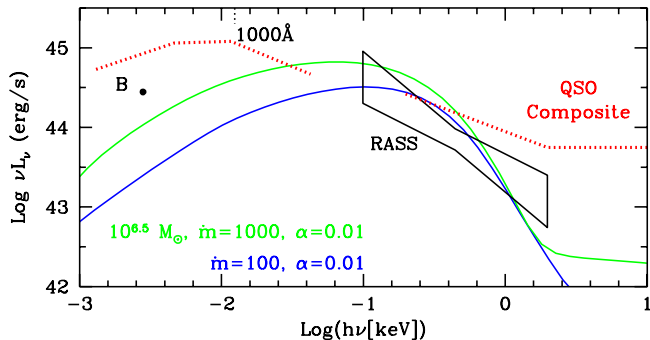


FIG. 14.— Comparison between the spectral models for NLS1s [solid lines; $\dot{m} = 100$ (lower) and 1000 (upper) with $M_{\text{BH}} = 10^{6.5} M_{\odot}$ and $\alpha = 0.01$] and the QSO composite spectrum (dotted lines; Zheng et al. 1997; Laor et al. 1997; Telmer et al. 2002). Observational data for PG 1448+273 are also shown for a presentation purpose. The two types of objects show quite different distributions. Extreme-UV luminosity is comparable in a NLS1 case ($\dot{m} = 1000$) and the QSO case, while optical and X-ray ones are so different.

6.5. Other Perspectives

As prescribed in §5, NLS1s can be in the younger phase of central BH formation/evolution. Mathur (2000) discuss the scenario in the context of gas content and metal richness of some NLS1s. If the “young AGN” hypothesis is the valid, NLS1s provide us a good sample for studying the evolution and formation of massive BHs residing in the center of galaxies. Kroengold, Dultzin-Hacyan & Marziani (2001) compared the environments of NLS1s with those of BLS1s based on the Digitized Sky Survey, finding no statistical difference between the two. We will need much better spatial resolution to observe disturbances on host galaxies that may feed BHs and ignite AGN activity, such as a ripple structure, tidal tail, nucleus bar and so on. Our forthcoming observation of nearby NLS1s with The University of Hawaii 2.2-meter telescope (PI; K. Aoki) will assess the validity of this idea.

With recent intensive studies, it has been established that mass of the galactic spheroid component (galactic bulge or elliptical galaxy itself) is strongly correlated with M_{BH} in inactive galaxies and AGNs (Gebhardt et al. 2000; Ferrarese & Merritt 2000; Nelson 2000). The tight correlation indicates that the growth of spheroid mass (in other words, formation of spheroids) and growth of M_{BH} (formation of BHs) are triggered by the same origin, or it implies that either controls the other growth/formation. The origin of the link is still unclear. Two, opposite, extremal ideas can be that i) Jet/Outflow due to gas accretion onto the central BH may govern the formation of spheroid (Silk & Rees 1998), i.e. BHs are made before the bulge growth; and ii) radiation drag by massive stars during the bulge formation can fuel the gas towards the central BH (Umemura 2001), resulting in bulges formed prior to BH

growth. Deep, optical/Near-IR, off-nuclear spectroscopic observations of spheroids (bulges) associated with the youngest AGNs will reveal the origin of the close correlation. The time-lag between the epochs of the bulge- and BH-growth could be recognized, depending on the spectral features of the bulges we shall obtain. It will promote insights into why the two massive, but with enormously different physical sizes, systems co-evolve.

7. SUMMARY

We have examined the effects of electron scattering (opacity and Comptonization) and the relativistic correction (gravitational redshift and transverse Doppler effect) on the emergent spectra from super-Eddington accretion flows (the so called slim disks) onto non-rotating BHs for $10^{1.5}$ and $10^{6.5} M_{\odot} M_{\text{BH}}$.

The effective optical depth of the flow can be less than unity for $\dot{m} [= \dot{M}/(L_{\text{Edd}}/c^2)] = 100 - 1000$ with $10^{1.5} M_{\odot}$ and for $\dot{m} = 100$ with $10^{6.5} M_{\odot}$, if $\alpha \geq 0.1$. An improvement in the knowledge of the cooling rate will be required in those parameter sets. Although \dot{m} -dependency and radial profile of each physical quantity in the super-Eddington flow are different from the standard disk, the M_{BH} -dependency of the two accretion modes are almost identical. The α -dependency is also similar, except for the innermost region ($r \lesssim 10r_{\text{Sch}}$). narrow-line QSOs will be desirable laboratories for studying the self-gravity of the flow via optical/Near-IR observations.

With $\dot{m} \geq 100$, the spectral hardening factor via electron scattering is $\sim 2.3 - 6.5$. The color temperature of the inner most radiation (T_{in}) is not proportional to $L^{0.25}$, as would be expected from the simplest standard accretion disk, due to the \dot{m} -sensitive spectral hardening factor. In the face-on view, there is no jump of T_{in} if we do not take the \dot{m} -sensitive electron scattering into account.

The improved spectral model has been applied to the optical-soft X-ray emission from NLS1s, for which M_{BH} are now estimated by a couple of ways, to evaluate their accretion rates \dot{m} . We have picked up one NLS1, PG 1448+273 with an inferred M_{BH} of $10^{6.4} M_{\odot}$, among the highest \dot{m} candidates. The broadband spectral distribution was successfully reproduced for the first time by the model with $\dot{m} = 1000$ and $\alpha = 0.01$.

This extremely high \dot{m} implies that this object, as well as some other highest \dot{m} systems, is really young: its inferred age (M_{BH}/\dot{M}) is less than 10^6 years.

We have also briefly discussed the accretion rate \dot{m} of transient and highly variable NLS1s, finding that those are located at $3 \lesssim \dot{m} \lesssim 300$. Such a moderately high accretion rate can indicate that this variability is relevant to the thermal instability. A possible type 2 counterpart of NLS1s, NGC 1068, seems to have \dot{m} similar to NLS1s.

A more accurate estimate for absorption opacity, for which we assume 30 times free-free opacity in this study for simplicity, is required for better spectral calculations. It is because the absorption opacity determines the location of the last thermalization surface, and hence the amount of redistributed photons by Comptonization. Also, viewing-angle dependent spectral models are needed.

This paper could never have been produced in this way without the use of the numerical code for solving the radial structure of super- and sub-Eddington accretion flows/disks that has been constructed and developed by Ryoji Matsumoto, Fumio Honma and Mitsu Takeuchi. The author wish to thank Karen

Leighly, Chiho Matsumoto, Ken-ya Watarai, Kentaro Aoki, Toshiya Shimura, Agata Różańska, Jerzy Madej, Bozena Czerny, Ed Baron, Jean-Marc Huré, Suzy Collin, Chris Done and Omer Blaes for helpful discussions. He also thanks Brandon Carter for patient and careful reading of the draft, Shin Mineshige for continuous encouragement, and an anonymous referee for careful reading and helpful comments. The main computations were performed at the Department of Physics and Astronomy of the University of Oklahoma, when the author was there as a visiting graduate student. He appreciates all the

member of the Department, especially C. Matsumoto and K. Leighly, for their hospitality. This research has made use of the NASA/IPAC Extragalactic Database (NED) which is operated by the Jet Propulsion Laboratory, California Institute of Technology, under contract with the National Aeronautics and Space Administration. This work was supported in part by the Research Fellowship of the Japan Society for the Promotion of Science (JSPS) for Young Scientists (4616), and by the JSPS Postdoctoral Fellowships for Research Abroad (464).

REFERENCES

Abramowicz M.A., Czerny B., Lasota J.P. & Szuszkiewicz E., 1988, *ApJ*, 332, 646
 Begelman M.C. & Meier D.L., 1982, *ApJ*, 253, 873
 Begelman M.C., 2001, *ApJ*, 551, 897
 Beloborodov A.M. 1998, *MNRAS* 297, 739
 Beloborodov A.M., Abramowicz M.A. & Novikov I.D. 1997, *ApJ*, 491, 267
 Bland-Hawthorn J., Sokolowski J. & Cecil G., 1991, *ApJ*, 375, 78
 Bland-Hawthorn J. & Voit G.M., 1993, *Rev. Mex. Astron. Astrofis.*, 27, 73
 Boller Th., Brandt W.N., Fink H.H. 1996, *A&A* 305, 53
 Boller Th., Brandt W.N., Fabian A.C., Fink H.H. 1997, *MNRAS* 289, 393
 Boroson, T. A. 2003, *ApJ*, 585, 647
 Brandt, W. N., Pounds, K. A., & Fink, H 1995, 273, L47
 Brandt W.N. & Gallagher S.C., 2000, *New Astronomy Reviews*, 44, 461
 Brandt W.N., Mathur S., Elvis M. 1997, *MNRAS* 285, L25
 Brandt W.N., Laor A. & Wills B.J., 2000, *ApJ*, 528, 637
 Brandt W.N., Boller Th., Fabian A.C., Ruszkowski 1999, *MNRAS* 303, L53
 Branduardi-Raymont, G., et al. 2001, *A&A*, 365, L140
 Burrows A.S., 1990, in *Supernovae* (Springer-Verlag) ed. A.G. Petschek, p.143
 Cheng L., Wei J. & Zhao Y., 2002, *Chinese J. Astron. Astrophys.*, 2, 207
 Colbert E. & Ptak A., 2002, *ApJS*, 143, 25
 Collin, S. et al. 2002, *A&A*, 388, 771
 Czerny, B. & Elvis, M. 1987, *ApJ*, 321, 305
 Dietrich M. & Wagner S.J., 1998, *A&A*, 338, 405
 Edelson R. et al., 1999, *MNRAS*, 307, 91
 Elizalde F. & Steiner J.E., 1994, *MNRAS*, 268, L47
 Ferrarese L. et al. 2001, *ApJL*, 555, 79
 Ferrarese L. & Merritt D. 2000, *ApJ*, 539, L9
 Forster, K. & Halpern, J.P., 1996, *ApJ*, 468, 565
 Fukue J. 2000, *PASJ*, 52, 829
 Gebhardt K. et al. 2000, *ApJ*, 539, L13
 Goldreich P. & Lynden-Bell D., *MNRAS*, 1965, 130, 97
 Greenhill L.J. & Gwinn C.R., 1997, *Ap&SS*, 248, 261
 Grupe, D., Beuermann, K., Mannheim, K., Bade, N., Thomas, H.-C., de Martino, D. & Schwone, A. 1995a, *A&A*, 299, L5
 Grupe, D., Beuermann, K., Mannheim, K., Thomas, H.-C., Fink, H. H., de Martino, D. 1995b, *A&A*, 300, L21
 Grupe G.D., Beuermann K., Thomas H.-C., Mannheim K. Fink H.H. 1998, *A&A* 330, 25
 Grupe G.D., Beuermann K., Mannheim K., Thomas H.-C. 1999, *A&A* 350, 805
 Grupe, G.D., Thomas H.-C. & Beuermann K., 2001, *A&A*, 367, 470
 Grupe G.D., Leighly K.M., Thomas H.-C., & Laurent-Muehleisen S.A. 2000, *A&A*, 356, 11
 Guainazzi, M., et al. 1998, *MNRAS*, 301, L1
 Halpern, J. P. & Oke, J. B. 1987, *ApJ* 312, 91
 Hayashida, K. 2000, *New Astron. Rev.*, 44, 419
 Honma F., Matsumoto R. & Kato S., 1991, *PASJ*, 43, 147
 Honma F., Matsumoto R., Kato S. & Abramowicz M.A., 1991, *PASJ*, 43, 261
 Hößl R., 1977, *Prog. Theor. Phys.*, 58, 1191
 Huré J.-M., 1998, *A&A*, 337, 625
 Janiuk A., Czerny B. & Siemiginowska A., 2002, *ApJ*, 576, 908
 Janka H.-T. & Hillebrandt W., 1989, *A&AS*, 78, 375
 Kaspi S., Smith P.S., Netzer H., Maoz D., Jannuzi B.T. & Giveon U. 2000, *ApJ*, 533, 631
 Kato S., Fukue J., & Mineshige S. 1998, *Black Hole Accretion Disks*, Kyoto Univ. Press
 Kawaguchi, T., Mineshige, S., Machida, M., Matsumoto, R., & Shibata, K. 2000, *PASJ*, 52, L1
 Kawaguchi, T., Pierens, A., & Huré, J.-M. 2003, *A&A*, submitted
 Korista K.T., 1991, *AJ*, 102, 41
 Krongold Y., Dultzin-Hacyan D. & Marziani P., 2001, *AJ*, 121, 702
 Kubota A., 2001, Ph.D. thesis, Univ. Tokyo
 Kubota A. et al. 2001a, *ApJ*, 547, L119
 Kubota A., Makishima K. & Ebisawa K., 2001b, *ApJ*, 560, L147
 Komossa S. & Bade N. 1999, *A&A*, 343, 775
 Laor, A., & Netzer, H. 1989, *MNRAS*, 238, 897
 Laor A., Fiore F., Elvis M., Wikes B. J. & McDowell J. C. 1997, *ApJ*, 477, 93
 Leighly, K. M. et al. 1996, *ApJ*, 469, 147
 Leighly, K. M. 1999a, *ApJS*, 125, 297
 Leighly, K. M. 1999b, *ApJS*, 125, 317
 Leighly, K. M., Zdziarski, A. A., Kawaguchi, T., & Matsumoto, C. 2002, in *X-ray Spectroscopy of AGN with Chandra and XMM-Newton*, ed. Th. Boller, S. Komossa, S. Kahn, & H. Kunieda (MPE Rep. 279; Garching: MPE), 259–262 (astro-ph/0205539)
 Liu B.F., Mineshige S., Meyer F., Meyer-Hofmeister E. & Kawaguchi T., 2002, *ApJ*, 575, 117
 Machida M., Hayashi M.R. & Matsumoto R., 2000, *ApJ*, 532, L67
 Madej J., 1974, *Acta Astronomica*, 24, 327
 Marshall H.L. et al., 1996, *ApJ*, 457, 169
 Marshall H.L., et al. , 2003, *AJ*, 125, 459
 Mason, K. O., et al. , 2003, *ApJ*, 582, 95
 Matsumoto R., Kato S., Fukue J., Okazaki A.T. 1984, *PASJ* 36, 71
 Matsumoto R., Kato S., Honma F., 1989, in *Theory of Accretion Disks*, eds. F. Meyer, W.J. Duschl, J. Frank, and E. Meyer-Hofmeister (Kluwer Academic Publishers, Dordrecht), p.167
 Mathur S., 2000, *MNRAS*, 314, L17
 Makishima K., et al. 2000, *ApJ*, 535, 632
 Mason K.O. et al., 1995, *MNRAS*, 274, 1194
 Meyer, F., & Meyer-Hofmeister, E., 1994, *A&A*, 288, 175
 Mezzacappa A. et al. 1998, *ApJ*, 493, 848
 Miller J.M., Fabbiano G., Miller M.C. & Fabian A.C., 2003, *ApJL*, 585, 37
 Miller J.S., Goodrich R.W. & Mathews W.G., 1991, *ApJ*, 378, 47
 Mineshige S., Kawaguchi T., Takeuchi M. & Hayashida K. 2000, *PASJ*, 52, 499
 Misra R. & Sriram K., 2003, *ApJ*, 584, 981
 Mitsuda K., et al., 1984, *PASJ*, 36, 741
 Mizuno T., Kubota A. & Makishima K., 2001, *ApJ*, 554, 1282
 Narayan R., Yi I. 1995, *ApJ* 444, 231
 Narayan R., 1997, in *Accretion Phenomena and Related Outflows*, Proc. IAU Colloq. 163, ASP Conf. series (eds. D.T. Wickramasinghe, G.V. Bicknell, L. Ferrario), p.75
 Nelson C.H. 2000, *ApJL*, 544, L91
 Ohsuga K., Mineshige S., Mori M. & Umemura M., 2002, *ApJ*, 574, 315
 Otani C., Kii T., Miya K. 1996 in *Röntgenstrahlung from the Universe* (MPE Report 263), ed H.U. Zimmermann, J.E. Trümper, H. Yorke (MPE Press, Garching) p491
 Osterbrock D.E., & Pogge R.W. 1985, *ApJ*, 297, 166
 Paczyński B., Witta P.J. 1980, *A&A* 88, 23
 Pakull, M. W., & Mirioni, L. 2002, in *New Visions of the X-ray Universe in the XMM-Newton and Chandra Era*, in press (astro-ph/0202488)
 Phillips M.M., 1976, *ApJ*, 208, 37
 Pier E.A. et al. 1994, *ApJ*, 428, 124
 Pogge R.W. 2000, *New Astronomy Reviews*, 44, 381
 Pounds K.A., Done C., Osborne J. 1995, *MNRAS* 277, L5
 Roberts T.P. & Warwick R.S., 2000, *MNRAS*, 315, 98
 Ross, R. R., Fabian, A. C., & Mineshige, S. 1992, *MNRAS*, 258, 189
 Rybicki, G. B., & Lightman, A. P. 1979, *Radiative Processes in Astrophysics*, John Wiley & Sons, New York
 Remillard R.A. et al., 1986, *ApJ*, 301, 742
 Savage B.D. & Mathis J.S., 1979, *ARA&A*, 17, 73
 Shakura N.I. & Sunyaev R.A., 1973, *A&A*, 24, 337
 Shimura, T., & Takahara, F. 1993, *ApJ*, 419, 78
 Shimura, T., & Takahara, F. 1995, *ApJ*, 445, 780
 Shimura, T., 2000, *MNRAS*, 315, 345
 Shimura, T., & Manmoto, T. 2003, *MNRAS*, 338, 1013
 Silk J. & Rees M., 1998, *A&A*, 331, L1
 Stirpe G.M., 1990, *A&AS*, 85, 1049
 Surace J.A., Sanders D.B. & Evans A.S., 2001, *AJ*, 122, 2791
 Svensson R., 1984, *MNRAS*, 209, 175
 Szuszkiewicz, E., Malkan, M. A., & Abramowicz, M. A. 1996, *ApJ*, 458, 474
 Tajiri Y., & Umemura M., 1998, *ApJ*, 502, 59
 Takeuchi, M. 2000, Poster contribution presented at the Joint MPE/AIP/ESO workshop on Observational and Theoretical Progress in the Study of Narrow-line Seyfert 1 Galaxies (astro-ph/0005162)
 Telfer R.C. et al. 2002, *ApJ*, 565, 773
 Umemura M., 2001, 2001, *ApJ*, 560, L29
 Uttley, P., McHardy, I.M., Papadakis, I. E., Guainazzi, M. & Fruscione, A., 1999, *MNRAS*, 307, L6

Vaughan S. et al. 2002, MNRAS, 337, 247
 Véron-Cetty M.P., Véron P. & Goncalves A.C., 2001, A&A, 372, 730
 Véron-Cetty M.P. & Véron P., 2001, A&A, 374, 92
 Walter R. & Fink H. H. 1993, A&A, 274, 105
 Wandel A., Peterson B.M. & Malkan M.A. 1999, ApJ, 526, 579
 Wandel A. & Petrosian V. 1988, ApJ, 329, L11
 Wang T., Brinkmann W. & Bergeron J. 1996, A&A, 309, 81
 Wang J.-M., Szuszkiewicz E., Lu F.-J. & Zhou Y.-Y., 1999, ApJ 522, 839
 Wang J.-M. & Netzer H., 2003, A&A, 398, 927
 Wang T. & Lu Y., 2001, A&A, 377, 52
 Watarai K., Fukue J., Takeuchi M. & Mineshige S., 2000, PASJ, 52, 133
 Watarai K., Mizuno T. & Mineshige S., 2001, ApJ, 549, L77
 Watarai K. & Mineshige S., 2001, PASJ, 53, 915
 Young A.J. et al., 1999, MNRAS, 304, L46
 Zheng, W., Kriss, G. A., Telfer, R. C., Grimes, J. P., & Davidsen, A. F. 1997, ApJ, 475, 469